SANDIA REPORT
SAND2007-0046
Unlimited Release
Printed January 2007

Wavefront Curvature Limitations and Compensation to Polar Format Processing for Synthetic Aperture Radar Images

Armin W. Doerry

Prepared by
Sandia National Laboratories
Albuquerque, New Mexico 87185 and Livermore, California 94550

Sandia is a multiprogram laboratory operated by Sandia Corporation,
a Lockheed Martin Company, for the United States Department of Energy's
National Nuclear Security Administration under Contract DE-AC04-94AL85000.

Issued by Sandia National Laboratories, operated for the United States Department of Energy by Sandia Corporation.

Available to DOE and DOE contractors from
U.S. Department of Energy
Office of Scientific and Technical Information
P.O. Box 62
Oak Ridge, TN 37831

Telephone: (865) 576-8401
Facsimile: (865) 576-5728
E-Mail: reports@adonis.osti.gov
Online ordering: http://www.osti.gov/bridge

Available to the public from
U.S. Department of Commerce
National Technical Information Service
5285 Port Royal Rd.
Springfield, VA 22161

Telephone: (800) 553-6847
Facsimile: (703) 605-6900
E-Mail: orders@ntis.fedworld.gov
Online order: http://www.ntis.gov/help/ordermethods.asp?loc=7-4-0#online

SAND2007-0046
Unlimited Release
Printed January 2007

Wavefront curvature limitations and compensation to Polar Format processing for Synthetic Aperture Radar images

Armin W. Doerry
SAR Applications Department

Sandia National Laboratories
PO Box 5800
Albuquerque, NM 87185-1330

ABSTRACT

Limitations on focused scene size for the Polar Format Algorithm (PFA) for Synthetic Aperture Radar (SAR) image formation are derived. A post processing filtering technique for compensating the spatially variant blurring in the image is examined. Modifications to this technique to enhance its robustness are proposed.

ACKNOWLEDGEMENTS

This work was funded by the US DOE Office of Nonproliferation & National Security, Office of Research and Development, NA-22, under the Advanced Radar System (ARS) project.

Sandia is a multiprogram laboratory operated by Sandia Corporation, a Lockheed Martin Company, for the United States Department of Energy under Contract DE-AC04-94AL85000.

CONTENTS

FOREWORD

Relatively recent Research & Development (R&D) radar systems built by Sandia National Laboratories, including its L/S-band Concealed Target SAR (CTSAR), Ka-band Ultra High Resolution SAR (UHRSAR), and Ku-band MiniSAR, have been operated in a manner to form images larger than the classical limits suggested for the Polar Format Algorithm (PFA). The desire for future operational systems to operate with ever larger images at ever finer resolutions exacerbate this problem. Consequently, Sandia is investigating techniques for extending the performance of its real-time systems, including mitigating the limitations of classical image formation techniques.

This effort began as an attempt to investigate the background of an existing post-processing wavefront curvature correction scheme. As is so often the case, pulling on a thread ultimately revealed a complex tapestry of issues and exploratory paths.

This report details an investigation into the limits of PFA processing, and explores an attractive mitigation scheme for wavefront curvature effects.

1 Introduction & Background

Synthetic Aperture Radar (SAR) is a technique whereby multiple pulses from a moving radar are coherently combined to form an image while achieving an azimuth resolution much finer than the beamwidth of the radar's real antenna. Range resolution is a function of radar signal bandwidth. Image formation is typically a computationally intensive operation. Consequently, transform techniques are favored that ultimately only approximate the matched filter for each pixel location in the image. The approximations tend to be most accurate at the image focal point, nominally its center.

Large scenes with relatively coarse resolutions tend to exhibit artifacts resulting from approximations to the spherical wavefronts. Small scenes at finer resolutions suffer more from range migration effects.

The Polar Format Algorithm (PFA) for spotlight SAR image formation was developed by Walker.[1] Its significance is that it recognizes that the raw Linear FM (LFM) SAR data, when de-chirped, represent sample points in the Fourier space of the scene being imaged, most accurately at the scene center, but suitably so for a significant neighborhood around the scene center, often for up to several thousand pixels depending on range and wavelength. At near ranges and longer wavelengths the focused image sizes may be substantially reduced. However, those raw data sample points are nominally on a polar grid in Fourier space, and need to be resampled to a rectangular grid for efficient processing with digital computers. This resampling is termed polar reformatting, hence the name Polar Format processing. The operation of PFA is adequately explained in a number of texts and publications, including the original paper by Walker,[1] texts by Carrera, et al.,[2] and Jakowatz, et al.,[3] and publications by Martin, et al.,[4] Martin and Doerry,[5] and Doerry.[6]

While the resampling of PFA mitigates the problematic range migration, residual effects of wavefront curvature still manifest themselves as spatially variant distortions and image quality degradation, generally worsening in the image with pixel distance from the scene center. In fact, a threshold on tolerance for image degradation imposes a scene size limit for a focused SAR image. This limit is addressed by Walker,[1] and refined by Doerry.[7]

Modern high-performance SAR systems now routinely operate with image dimensions of several thousand pixels by several thousand pixels that often exceed the focused scene size limits for PFA processing.

Subaperture techniques combined with PFA have been shown by Doerry[8,9,10] to effectively mitigate wavefront curvature effects and substantially increase focused scene diameter. This is a class of image formation algorithms and is generally not suitable for application to an already processed image, unless the original image formation processing is first undone.

More recently, a technique for post-processing PFA images has been reported that applies a spatially variant filter to an already formed image, thereby correcting the misfocus due to residual wavefront curvature effects. Papers by Doren, et al.,[11] and Jakowatz, et al.,[12] as well as a detailed report/dissertation by Doren,[13] detail the principles of what they term Polar Formatting with Post Filtering (PF2) processing. However, the technique as detailed suffers in its robustness over imaging geometry, being designed for a linear flight path, and may in fact actually increase phase errors in other circumstances. Doren in his dissertation acknowledges that "For optimal versatility, the wavefront curvature compensation could be extended to apply to phase histories generated by flying an arbitrary flight path."

This report examines in detail the limitations of PFA, and proposes a somewhat more robust post-processing filter for wavefront curvature correction.

2 Overview & Summary

PFA processing is an approximation to a matched filter for the pixel locations in a SAR image. The degree to which PFA matches the ideal matched filter diminishes as pixel locations are increasingly distant from the focused image center. The manifestation of this non-idealness is a spatially variant distortion and misfocus in the image. This non-idealness is deterministic, and can be corrected with spatially variant filters of the image.

Geometric distortions can be corrected by image warping. A technique has been reported in the literature for applying a spatially variant filter to an image to correct for the misfocus due to wavefront curvature. The reported technique is still an approximation, and was designed presuming a straight-line flight path. It consequently has limitations with respect to other imaging geometries, and may actually worsen an image under some circumstances.

Herein is reported a detailed derivation of PFA limitations and wavefront curvature effects correction. The proposed modification to the spatially variant filter is more comprehensive than existing post-processing techniques.

A fundamental result is that the nature of the phase error due to waveform curvature depends on the specific flight path of the radar, and hence any robust correction scheme needs to depend on the specific flight path as well.

“A person with a new idea is a crank until the idea succeeds.”

Mark Twain

3 Detailed Analysis

3.1 The video phase history data model

Consider a LFM transmitted signal of the form

$$X_T(t,n) = A_T \,\mathrm{rect}\left(\frac{t-t_n}{T}\right)\exp\, j\left\{\phi_{T,n} + \omega_{T,n}(t-t_n) + \frac{\gamma_{T,n}}{2}(t-t_n)^2\right\} \tag{1}$$

where

A_T = the amplitude of the transmitted pulse,
t = time,
n = index value of pulse number, $-N/2 \le n < N/2$,
t_n = reference time of nth pulse,
T = transmitted pulse width,
$\phi_{T,n}$ = transmit waveform reference phase of nth pulse,
$\omega_{T,n}$ = transmit waveform reference frequency of nth pulse, and
$\gamma_{T,n}$ = transmit waveform chirp rate of nth pulse. (2)

The received echo from a point scatterer is a delayed and attenuated version of this, namely

$$X_R(t,n) = \frac{A_R}{A_T} X_T(t - t_{s,n}, n) \tag{3}$$

where

A_R = the amplitude of the received pulse,
$t_{s,n}$ = echo delay time of the received echo for the nth pulse. (4)

This is expanded to

$$X_R(t,n) = A_R \,\mathrm{rect}\left(\frac{t-t_n-t_{s,n}}{T}\right)\exp\, j\left\{\phi_{T,n} + \omega_{T,n}(t-t_n-t_{s,n}) + \frac{\gamma_{T,n}}{2}(t-t_n-t_{s,n})^2\right\}. \tag{5}$$

Employing stretch processing, and Quadrature demodulation, requires mixing this with a Local Oscillator (LO) signal of the form

$$X_L(t,n) = \text{rect}\left(\frac{t - t_n - t_{m,n}}{T_L}\right) \exp j\left\{\phi_{L,n} + \omega_{L,n}\left(t - t_n - t_{m,n}\right) + \frac{\gamma_{L,n}}{2}\left(t - t_n - t_{m,n}\right)^2\right\} \tag{6}$$

where

$t_{m,n}$ = reference delay time of nth LO pulse,
T_L = LO pulse width,
$\phi_{L,n}$ = LO waveform reference phase of nth LO pulse,
$\omega_{L,n}$ = LO waveform reference frequency of nth LO pulse, and
$\gamma_{L,n}$ = LO waveform chirp rate of nth LO pulse. (7)

This yields a baseband video signal of the form

$$X_V(t,n) = X_R(t,n) X_L(t,n)^* \tag{8}$$

or

$$X_V(t,n) = \left[\begin{array}{l} A_R \,\text{rect}\left(\dfrac{t - t_n - t_{s,n}}{T}\right)\text{rect}\left(\dfrac{t - t_n - t_{m,n}}{T_L}\right) \\ \times \exp j\left\{\begin{array}{l} \phi_{T,n} + \omega_{T,n}\left(t - t_n - t_{s,n}\right) + \dfrac{\gamma_{T,n}}{2}\left(t - t_n - t_{s,n}\right)^2 \\ -\phi_{L,n} - \omega_{L,n}\left(t - t_n - t_{m,n}\right) - \dfrac{\gamma_{L,n}}{2}\left(t - t_n - t_{m,n}\right)^2 \end{array}\right\} \end{array}\right] \tag{9}$$

which simplifies to

$$X_V(t,n) = \left[\begin{array}{l} A_R \,\text{rect}\left(\dfrac{t - t_n - t_{s,n}}{T}\right)\text{rect}\left(\dfrac{t - t_n - t_{m,n}}{T_L}\right) \\ \times \exp j\left\{\begin{array}{l} \phi_{T,n} - \phi_{L,n} \\ + \omega_{T,n}\left(t - t_n - t_{s,n}\right) - \omega_{L,n}\left(t - t_n - t_{m,n}\right) \\ + \dfrac{\gamma_{T,n}}{2}\left(t - t_n - t_{s,n}\right)^2 - \dfrac{\gamma_{L,n}}{2}\left(t - t_n - t_{m,n}\right)^2 \end{array}\right\} \end{array}\right]. \tag{10}$$

In this model, we presume

$$\phi_{L,n} = \phi_{T,n},$$
$$\omega_{L,n} = \omega_{T,n},$$
$$\gamma_{L,n} = \gamma_{T,n}, \tag{11}$$

which allows the reduction to

$$X_V(t,n) = \left[\begin{array}{l} A_R \,\mathrm{rect}\left(\dfrac{t - t_n - t_s}{T} \right) \mathrm{rect}\left(\dfrac{t - t_n - t_m}{T_L} \right) \\ \times \exp j\left\{ \left(\omega_{T,n} + \gamma_{T,n}\left(t - t_n - t_m\right) \right)\left(t_m - t_s\right) + \dfrac{\gamma_{T,n}}{2}\left(t_m - t_s\right)^2 \right\} \end{array} \right]. \tag{12}$$

Now let

$$t_{m,n} = t_{c,n} = \frac{2}{c}\left|\mathbf{r}_{c,n}\right|,$$
$$t_{s,n} = \frac{2}{c}\left|\mathbf{r}_{s,n}\right|,$$
$$\left(t - t_n - t_{c,n}\right) = \left(iT_{s,n} + \tau_n\right) \text{ for } -I/2 \le i < I/2, \tag{13}$$

where

$\mathbf{r}_{c,n}$ = the position vector of the radar with respect to the target scene center,
$\mathbf{r}_{s,n}$ = the position vector of the radar with respect to the target point,
i = the intra-pulse data index,
$T_{s,n}$ = the intra-pulse sampling interval, and
τ_n = the intra-pulse sampling delay. (14)

which allows the sampled video data to be described as

$$X_V(i,n) = A_R \exp j\left\{ \left(\omega_{T,n} + \gamma_{T,n}\tau_n + \gamma_{T,n}T_{s,n}i \right)\frac{2}{c}\left(\left|\mathbf{r}_{c,n}\right| - \left|\mathbf{r}_{s,n}\right| \right) + \frac{2\gamma_{T,n}}{c^2}\left(\left|\mathbf{r}_{c,n}\right| - \left|\mathbf{r}_{s,n}\right| \right)^2 \right\}. \tag{15}$$

Letting

$$r_{cs,n} = \left(\left|\mathbf{r}_{c,n}\right| - \left|\mathbf{r}_{s,n}\right| \right) \tag{16}$$

Allows us to write

$$X_V(i,n) = A_R \exp j\left\{\left(\omega_{T,n} + \gamma_{T,n}\tau_n + \gamma_{T,n}T_{s,n}i\right)\frac{2}{c}r_{cs,n} + \frac{2\gamma_{T,n}}{c^2}{r_{cs,n}}^2\right\}. \quad (17)$$

It becomes convenient to constrain

$$\left(\omega_{T,n} + \gamma_{T,n}\tau_n + \gamma_{T,n}T_{s,n}i\right) = \kappa_n\left(\omega_0 + \gamma_0 T_{s,0}i\right) \quad (18)$$

where

ω_0 = the nominal or reference frequency,
γ_0 = the nominal or reference chirp rate, and
$T_{s,0}$ = the nominal or reference sample spacing, (19)

which allows

$$X_V(i,n) = A_R \exp j\left\{\frac{2}{c}\left(\omega_0 + \gamma_0 T_{s,0}i\right)\kappa_n r_{cs,n} + \frac{2\gamma_{T,n}}{c^2}{r_{cs,n}}^2\right\}. \quad (20)$$

The second phase term is known as the residual video phase error and can be removed by data preprocessing, but can also often be ignored. Ignoring the RSPE will slightly degrade the image, and result in a slightly smaller focused scene diameter, the degree of which is exacerbated by short pulses with high chirp rates.

PFA Processing

The details and variations of PFA processing are adequately addressed in a number of other texts and reports. Figure 1 illustrates one set of processing steps that accomplishes this.

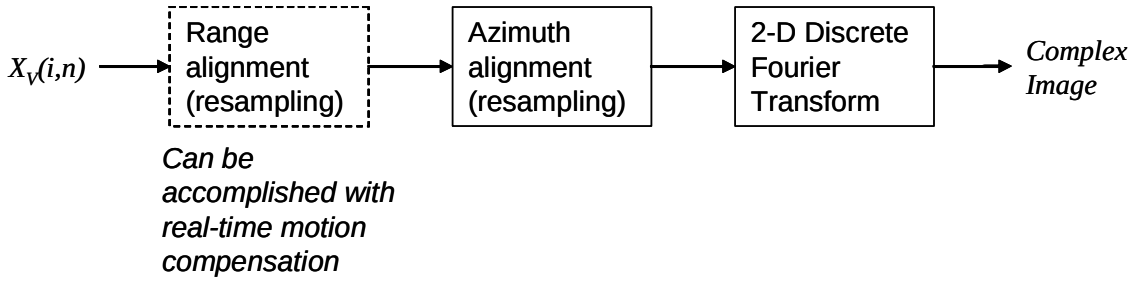

Figure 1. Typical PFA processing chain.

Removing Residual Video Phase Error (RVPE)

Removing the RVPE (also known as deskewing) entails filtering the data in the range dimension, and can be accomplished in the frequency domain by a Fourier Transform

across index *i*, followed by a phase correction, followed by an inverse Fourier Transform in the following manner. The technique is discussed in texts by both by Carrera, et al.,[2] and Jakowatz, et al.[3] We repeat the technique here for completeness.

We first rewrite the video data as

$$X_V(i,n) = A_R \exp j\left\{\frac{2}{c}\omega_0\kappa_n r_{cs,n} + \frac{2\gamma_{T,n}}{c^2} r_{cs}{}^2 + \frac{2}{c}\gamma_0 T_{s,0}\kappa_n r_{cs,n} i\right\}. \tag{21}$$

Then the Discrete Fourier Transform (DFT) across index *i* is defined as

$$X_V(v,n) = DFT_i\left(X_V(i,n)\right) = \sum_i X_V(i,n)\exp j\left\{-2\pi\frac{v}{V}i\right\}. \tag{22}$$

To facilitate the subsequent discussion, we note that with index *i* such that $-I/2 \le i < I/2$, the Discrete Fourier Transform of an exponential is given by

$$DFT_i\left(\exp j\{\Omega i\}\right) = \sum_i \exp j\{\Omega i\}\exp j\left\{-2\pi\frac{v}{V}i\right\} = \mathrm{csinc}_V\left(\frac{V}{2}\left(\Omega - \frac{2\pi}{V}v\right)\right) \tag{23}$$

where

$$\mathrm{csinc}_V(x) = \frac{\sin(x)}{\sin(x/V)}\exp j\left(-\frac{x}{V}\right). \tag{24}$$

Consequently,

$$X_V(v,n) = A_R \exp j\left\{\frac{2}{c}\omega_0\kappa_n r_{cs,n} + \frac{2\gamma_{T,n}}{c^2} r_{cs,n}{}^2\right\} DFT_i\left(\exp j\left\{\frac{2}{c}\gamma_0 T_{s,0}\kappa_n r_{cs,n} i\right\}\right) \tag{25}$$

or

$$X_V(v,n) = A_R \exp j\left\{\frac{2}{c}\omega_0\kappa_n r_{cs,n} + \frac{2\gamma_{T,n}}{c^2} r_{cs,n}{}^2\right\} \mathrm{csinc}_V\left(\frac{V}{2}\left(\frac{2}{c}\gamma_0 T_{s,0}\kappa_n r_{cs,n} - \frac{2\pi}{V}v\right)\right). \tag{26}$$

Note that the nature of the csinc function is to force a correspondence between $r_{cs,n}$ and index *v*, such that for each index *v* we may estimate

$$\hat{r}_{cs,n} = \frac{2\pi}{V}\left(\frac{c}{2\gamma_0 T_{s,0}\kappa_n}\right)v. \tag{27}$$

This allows us to compensate the RVPE by a point-by-point phase correction of

$$X'_V(v,n) = X_V(v,n)\exp j\left\{-\frac{2\gamma_{T,n}}{c^2}\hat{r}_{cs,n}{}^2\right\} \tag{28}$$

or

$$X'_V(v,n) \approx A_R \exp j\left\{\frac{2}{c}\omega_0\kappa_n r_{cs,n}\right\}\text{csinc}_V\left(\frac{V}{2}\left(\frac{2}{c}\gamma_0 T_{s,0}\kappa_n r_{cs,n} - \frac{2\pi}{V}v\right)\right). \tag{29}$$

Performing an Inverse DFT (IDFT) on the corrected data results in a video signal with the RVPE compensated, namely

$$X_V(i,n) = A_R \exp j\left\{\frac{2}{c}\omega_0\kappa_n r_{cs,n} + \frac{2}{c}\gamma_0 T_{s,0}\kappa_n r_{cs,n} i\right\}. \tag{30}$$

Consequently, whether ignored or compensated, this leaves us with a data model of

$$X_V(i,n) = A_R \exp j\left\{\frac{2}{c}\left(\omega_0 + \gamma_0 T_{s,0} i\right)\kappa_n r_{cs,n}\right\}. \tag{31}$$

These steps are illustrated in Figure 2.

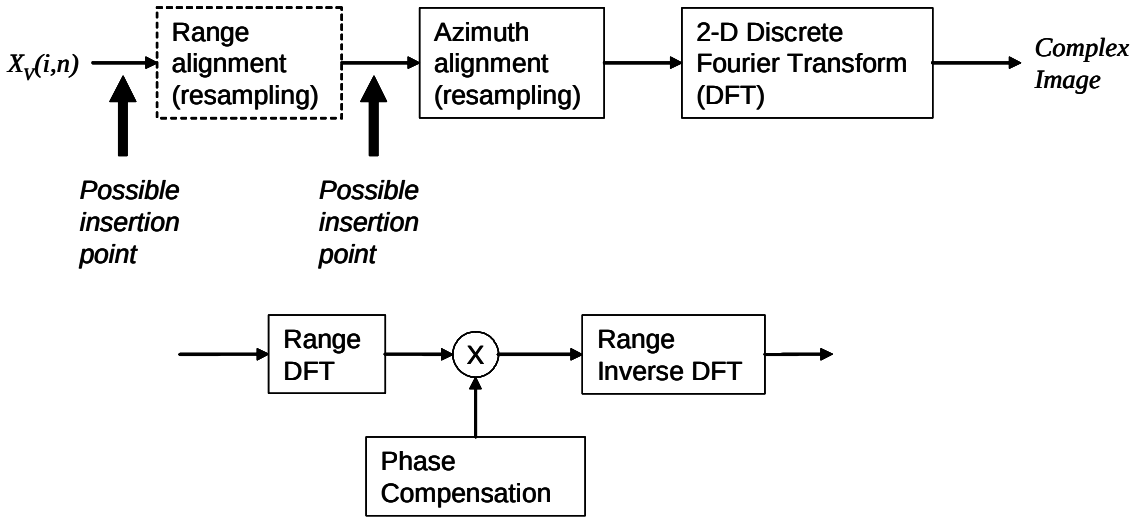

Figure 2. RVPE compensation steps and insertion points into PFA processing.

3.2 The target scene

Consider the geometry of Figure 3 where

$\mathbf{s}$ = the target scatterer location vector from the scene center,
$\psi_{c,n}$ = the grazing angle at the scene center, and
α_n = the instantaneous aperture viewing angle. (32)

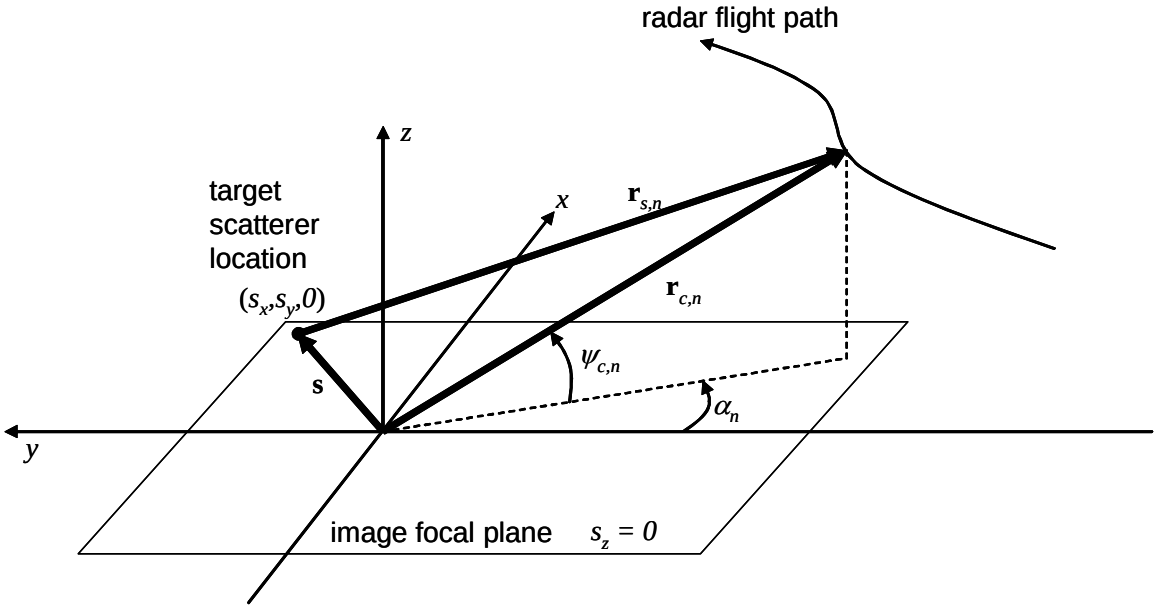

Figure 3. Radar geometry definitions.

Note that

$$\left|\mathbf{r}_{s,n}\right| = \left|\mathbf{r}_{c,n} - \mathbf{s}\right| \tag{33}$$

which allows

$$r_{cs,n} = \left|\mathbf{r}_{c,n}\right| - \left|\mathbf{r}_{s,n}\right| = \left|\mathbf{r}_{c,n}\right| - \left|\mathbf{r}_{c,n} - \mathbf{s}\right|. \tag{34}$$

In general, $\mathbf{r}_{c,n}$ and $\mathbf{r}_{s,n}$ vary with index *n*. This in fact defines the synthetic aperture.

However

$$\left|\mathbf{r}_{c,n} - \mathbf{s}\right| = \sqrt{\left|\mathbf{r}_{c,n} - \mathbf{s}\right|^2} = \sqrt{\left(\mathbf{r}_{c,n} - \mathbf{s}\right) \bullet \left(\mathbf{r}_{c,n} - \mathbf{s}\right)} = \sqrt{\left|\mathbf{r}_{c,n}\right|^2 - 2\mathbf{r}_{c,n} \bullet \mathbf{s} + \left|\mathbf{s}\right|^2} \tag{35}$$

or, more conveniently,

$$\left|\mathbf{r}_{c,n}-\mathbf{s}\right|=\left|\mathbf{r}_{c,n}\right|\sqrt{1-\frac{2\mathbf{r}_{c,n}\bullet\mathbf{s}}{\left|\mathbf{r}_{c,n}\right|^2}+\frac{\left|\mathbf{s}\right|^2}{\left|\mathbf{r}_{c,n}\right|^2}}=\left|\mathbf{r}_{c,n}\right|\sqrt{1-\frac{2\mathbf{n}_{c,n}\bullet\mathbf{s}}{\left|\mathbf{r}_{c,n}\right|}+\frac{\left|\mathbf{s}\right|^2}{\left|\mathbf{r}_{c,n}\right|^2}} \tag{36}$$

where $\mathbf{r}_{c,n}=\left|\mathbf{r}_{c,n}\right|\mathbf{n}_{c,n}$.

By using the expansion

$$\sqrt{1+a}=1+\frac{a}{2}-\frac{a^2}{8}+... \tag{37}$$

we can write

$$\left|\mathbf{r}_{c,n}-\mathbf{s}\right|=\left|\mathbf{r}_{c,n}\right|\left(1+\frac{-\frac{2\mathbf{n}_{c,n}\bullet\mathbf{s}}{\left|\mathbf{r}_{c,n}\right|}+\frac{\left|\mathbf{s}\right|^2}{\left|\mathbf{r}_{c,n}\right|^2}}{2}-\frac{\left(-\frac{2\mathbf{n}_{c,n}\bullet\mathbf{s}}{\left|\mathbf{r}_{c,n}\right|}+\frac{\left|\mathbf{s}\right|^2}{\left|\mathbf{r}_{c,n}\right|^2}\right)^2}{8}+...\right) \tag{38}$$

or

$$\left|\mathbf{r}_{c,n}-\mathbf{s}\right|=\left(\left|\mathbf{r}_{c,n}\right|-\left(\mathbf{n}_{c,n}\bullet\mathbf{s}\right)+\frac{\left|\mathbf{s}\right|^2}{2\left|\mathbf{r}_{c,n}\right|}-\frac{\left(\mathbf{n}_{c,n}\bullet\mathbf{s}\right)^2}{2\left|\mathbf{r}_{c,n}\right|}+\frac{\left(\mathbf{n}_{c,n}\bullet\mathbf{s}\right)}{2}\frac{\left|\mathbf{s}\right|^2}{\left|\mathbf{r}_{c,n}\right|^2}-\frac{\left|\mathbf{s}\right|^4}{8\left|\mathbf{r}_{c,n}\right|^3}+...\right) \tag{39}$$

which yields

$$r_{cs,n}=\left(\mathbf{n}_{c,n}\bullet\mathbf{s}\right)+\frac{\left(\mathbf{n}_{c,n}\bullet\mathbf{s}\right)^2}{2\left|\mathbf{r}_{c,n}\right|}-\frac{\left|\mathbf{s}\right|^2}{2\left|\mathbf{r}_{c,n}\right|}-\frac{\left(\mathbf{n}_{c,n}\bullet\mathbf{s}\right)}{2}\frac{\left|\mathbf{s}\right|^2}{\left|\mathbf{r}_{c,n}\right|^2}+\frac{\left|\mathbf{s}\right|^4}{8\left|\mathbf{r}_{c,n}\right|^3}-.... \tag{40}$$

Conventional PFA simplifies this to just the first term, but acknowledges the second term as the principal source of residual phase error limiting the focused scene diameter. Terms beyond this are almost always just outright ignored. We shall see that this leads to some significant errors.

For this treatment, we write

$$r_{cs,n}=\left(\mathbf{n}_{c,n}\bullet\mathbf{s}\right)+r_{pe,n} \tag{41}$$

and identify the complete range error as

$$r_{pe,n} = r_{cs,n} - \left(\mathbf{n}_{c,n} \bullet \mathbf{s}\right) = \left|\mathbf{r}_{c,n}\right| \left(1 - \sqrt{1 - \frac{2\mathbf{n}_{c,n} \bullet \mathbf{s}}{\left|\mathbf{r}_{c,n}\right|} + \frac{\left|\mathbf{s}\right|^2}{\left|\mathbf{r}_{c,n}\right|^2}} \right) - \left(\mathbf{n}_{c,n} \bullet \mathbf{s}\right). \tag{42}$$

The phase error

The video signal data model can then be written as

$$X_V(i,n) = A_R \exp j\left\{ \frac{2}{c}\left(\omega_0 + \gamma_0 T_{s,0} i\right)\kappa_n \left(\left(\mathbf{n}_{c,n} \bullet \mathbf{s}\right) + r_{pe,n} \right) \right\} \tag{43}$$

and further expanded to

$$X_V(i,n) = A_R \exp j\left\{ \frac{2}{c}\left(\omega_0 + \gamma_0 T_{s,0} i\right)\kappa_n \left(\mathbf{n}_{c,n} \bullet \mathbf{s}\right) + \phi_{pe,n} \right\} \tag{44}$$

where

$$\phi_{pe,n} = \frac{2}{c}\left(\omega_0 + \gamma_0 T_{s,0} i\right)\kappa_n r_{pe,n}\,. \tag{45}$$

Note that our notation does not explicitly show that $\phi_{pe,n}$ is also a function of index *i*, but this dependence nevertheless also exists, and will ultimately be shown to be significant for some purposes. For now we allow this dependence to be stealthy.

3.3 Conventional development of focused scene diameter limits

As previously stated, the usual approximation for the range error is

$$r_{pe,n} \approx \frac{\left(\mathbf{n}_{c,n} \bullet \mathbf{s}\right)^2}{2\left|\mathbf{r}_{c,n}\right|}. \tag{46}$$

From the geometry we also note that for a flat target scene

$$\left(\mathbf{n}_{c,n} \bullet \mathbf{s}\right) = s_x \cos\psi_{c,n} \sin\alpha_n - s_y \cos\psi_{c,n} \cos\alpha_n = \cos\psi_{c,n} \cos\alpha_n \left(s_x \tan\alpha_n - s_y\right) \tag{47}$$

and consequently

$$r_{pe,n} \approx \frac{\left(\cos\psi_{c,n} \cos\alpha_n \left(s_x \tan\alpha_n - s_y\right)\right)^2}{2\left|\mathbf{r}_{c,n}\right|} = \frac{\cos^2\psi_{c,n} \cos^2\alpha_n \left(s_x \tan\alpha_n - s_y\right)^2}{2\left|\mathbf{r}_{c,n}\right|}. \tag{48}$$

We note that $r_{pe,n}$ can also be expanded to

$$r_{pe,n} \approx \frac{\cos^2\psi_{c,n} \left(s_x{}^2 \sin^2\alpha_n + s_y{}^2 \cos^2\alpha_n - 2s_x s_y \sin\alpha_n \cos\alpha_n\right)}{2\left|\mathbf{r}_{c,n}\right|} \tag{49}$$

or

$$r_{pe,n} \approx \frac{\cos^2\psi_{c,n} \left(s_x{}^2 \sin^2\alpha_n + s_y{}^2 \left(1 - \sin^2\alpha_n\right) - 2s_x s_y \sin\alpha_n \cos\alpha_n\right)}{2\left|\mathbf{r}_{c,n}\right|} \tag{50}$$

or

$$r_{pe,n} \approx \frac{\cos^2\psi_{c,n} \left(\left(s_x{}^2 - s_y{}^2\right)\sin^2\alpha_n + s_y{}^2 - 2s_x s_y \sin\alpha_n \cos\alpha_n\right)}{2\left|\mathbf{r}_{c,n}\right|}. \tag{51}$$

Small angle approximations yield

$$r_{pe,n} \approx \left(\frac{1}{2\left|\mathbf{r}_{c,n}\right|}\right)\left(\cos^2\psi_{c,n} \left(s_x{}^2 - s_y{}^2\right)\alpha_n{}^2 - 2s_x s_y \cos^2\psi_{c,n} \left(1 - \frac{\alpha_n{}^2}{2}\right)\alpha_n + s_y{}^2 \cos^2\psi_{c,n}\right). \tag{52}$$

For focused scene diameter analysis, this is often further reduced to the term

$$r_{pe,n} \approx \frac{\cos^2 \psi_{c,n} \left({s_x}^2 - {s_y}^2 \right)}{2\left|\mathbf{r}_{c,n}\right|} {\alpha_n}^2 . \tag{53}$$

When inserted into the expression for phase error, and ignoring the dependence on range index *i*, this becomes the phase error term

$$\phi_{pe,n} = \frac{2\omega_0}{c} \kappa_n \frac{\cos^2 \psi_{c,n} \left({s_x}^2 - {s_y}^2 \right)}{2\left|\mathbf{r}_{c,n}\right|} {\alpha_n}^2 . \tag{54}$$

The conventional further simplification for finding maximum scene size includes

$$\begin{aligned} &\left(\frac{\omega_0}{c} \right) = \frac{2\pi}{\lambda_0}, \\ &\kappa_n = 1, \\ &\cos\psi_{c,n} = \cos\psi_{c,0}, \\ &\left|\mathbf{r}_{c,n}\right| = \left|\mathbf{r}_{c,0}\right|, \end{aligned} \tag{55}$$

where

$$\begin{aligned} &\lambda_0 \text{ = the nominal wavelength of the radar waveform, and} \\ &\psi_{c,0} \text{ = the nominal reference grazing angle.} \end{aligned} \tag{56}$$

This is tantamount to assuming a synthetic aperture that is a segment of a horizontal circular flight path orbiting the scene center, with fixed range and grazing angle. We shall later see that these assumptions can be problematic for other imaging geometries.

These assumptions and corresponding substitutions cause the phase error term to become quadratic, that is, we identify the quadratic phase error as

$$\phi_{qpe,n} = \left(\frac{2\pi}{\lambda_0} \right) \cos^2 \psi_{c,0} \frac{\left({s_x}^2 - {s_y}^2 \right)}{2\left|\mathbf{r}_{c,0}\right|} {\alpha_n}^2 . \tag{57}$$

The common derivation of maximum scene diameter is calculated along the cardinal axes passing through the scene center, and equates

$$\begin{aligned} &{s_x}^2 \le \left(\frac{D_x}{2} \right)^2 \text{ when } s_y = 0, \\ &{s_y}^2 \le \left(\frac{D_y}{2} \right)^2 \text{ when } s_x = 0, \\ &{\alpha_n}^2 \le \left(\frac{\lambda_0}{4\rho_x \cos\psi_{c,0}} \right)^2, \end{aligned} \tag{58}$$

where

ρ_x = the nominal azimuth resolution of the radar. (59)

For azimuth scene diameter D_x we require the constraint

$$\left\{\left(\frac{2\pi}{\lambda_0}\right)\cos^2\psi_{c,0}\left(\frac{\left(\frac{D_x}{2}\right)^2}{|\mathbf{r}_{c,0}|}\right)\left(\frac{\lambda_0}{4\rho_x\cos\psi_{c,0}}\right)^2\right\} \le \phi_{qpe,\max} \tag{60}$$

which reduces to

$$D_x{}^2 \le (4\rho_x)^2\left(\frac{|\mathbf{r}_{c,0}|}{\lambda_0}\right)\left(\frac{\phi_{qpe,\max}}{\frac{\pi}{2}}\right), \tag{61}$$

or the more familiar

$$D_x \le (4\rho_x)\sqrt{\left(\frac{|\mathbf{r}_{c,0}|}{\lambda_0}\right)\left(\frac{\phi_{qpe,\max}}{\frac{\pi}{2}}\right)}. \tag{62}$$

In a similar fashion, for range scene diameter

$$D_y \le (4\rho_x)\sqrt{\left(\frac{|\mathbf{r}_{c,0}|}{\lambda_0}\right)\left(\frac{\phi_{pe,\max}}{\frac{\pi}{2}}\right)}. \tag{63}$$

These are the commonly quoted (and accepted) limits for PFA processing. We shall see in the next section that this is often too simplistic.

Also, these limits can be written in terms of number of pixels as

$$\begin{aligned} P_x &= \frac{D_x}{\rho_x/a_{os,x}} \le 4a_{os,x}\sqrt{\left(\frac{|\mathbf{r}_{c,0}|}{\lambda_0}\right)\left(\frac{\phi_{qpe,\max}}{\frac{\pi}{2}}\right)}, \\ P_y &= \frac{D_y}{\rho_y/a_{os,y}} \le 4a_{os,y}\left(\frac{\rho_x}{\rho_y}\right)\sqrt{\left(\frac{|\mathbf{r}_{c,0}|}{\lambda_0}\right)\left(\frac{\phi_{qpe,\max}}{\frac{\pi}{2}}\right)}, \end{aligned} \tag{64}$$

where

$a_{os,x}$ = the ratio of resolution to pixel spacing in azimuth, and
$a_{os,y}$ = the ratio of resolution to pixel spacing in range. (65)

This derivation also presumed that no window functions or other aperture tapering was used for sidelobe control. Doing so would have necessitated extending the synthetic aperture fractionally to accommodate the broadening of the Impulse Response (IPR).

To incorporate the IPR broadening requires substituting

$$\rho_x \rightarrow \left(\frac{\rho_x}{a_{w,x}} \right) \tag{66}$$

where $a_{w,x}$ is the IPR broadening factor.

We end this section with the comment that Walker[1] developed PFA processing in terms of a rotating target scene that essentially corresponded to a circular flight path.

3.4 Real time motion compensation effects on scene diameter limits – circular flight path

Recall that we identified

$$X_V(i,n) = A_R \exp j\left\{\frac{2}{c}\left(\omega_0 + \gamma_0 T_{s,0} i\right)\kappa_n\left(\mathbf{n}_{c,n} \bullet \mathbf{s}\right) + \phi_{pe,n}\right\} \tag{67}$$

which we now expand to

$$X_V(i,n) = A_R \exp j\left\{\frac{2}{c}\left(\omega_0 + \gamma_0 T_{s,0} i\right)\kappa_n \cos\psi_{c,n} \cos\alpha_n\left(s_x \tan\alpha_n - s_y\right) + \phi_{pe,n}\right\}. \tag{68}$$

Real-time motion compensation allows us to effect

$$\kappa_n \cos\psi_{c,n} \cos\alpha_n = \cos\psi_{c,0} \tag{69}$$

such that

$$X_V(i,n) = A_R \exp j\left\{\frac{2}{c}\left(\omega_0 + \gamma_0 T_{s,0} i\right)\cos\psi_{c,0}\left(s_x \tan\alpha_n - s_y\right) + \phi_{pe,n}\right\}. \tag{70}$$

While termed real-time motion compensation, this is a fundamental operation for polar reformatting, and needs to be accomplished in any case, whether by real-time parameter manipulation, or by data interpolation after the fact.

In this case, the phase error becomes

$$\phi_{pe,n} = \frac{2}{c}\left(\omega_0 + \gamma_0 T_{s,0} i\right)\frac{\cos\psi_{c,0}}{\cos\psi_{c,n}\cos\alpha_n} r_{pe,n}. \tag{71}$$

As previously stated, the usual approximation for the range error is

$$r_{pe,n} \approx \frac{\left(\mathbf{n}_{c,n} \bullet \mathbf{s}\right)^2}{2\left|\mathbf{r}_{c,n}\right|} \tag{72}$$

however for this development we will carry along an extra term, and use the approximation

$$r_{pe,n} \approx \frac{\left(\mathbf{n}_{c,n} \bullet \mathbf{s}\right)^2}{2\left|\mathbf{r}_{c,n}\right|} - \frac{\left|\mathbf{s}\right|^2}{2\left|\mathbf{r}_{c,n}\right|} = \frac{\left(\mathbf{n}_{c,n} \bullet \mathbf{s}\right)^2 - \left|\mathbf{s}\right|^2}{2\left|\mathbf{r}_{c,n}\right|}. \tag{73}$$

From the geometry we also recall that for a flat target scene

$$\left(\mathbf{n}_{c,n} \bullet \mathbf{s}\right) = s_x \cos\psi_{c,n} \sin\alpha_n - s_y \cos\psi_{c,n} \cos\alpha_n = \cos\psi_{c,n} \cos\alpha_n \left(s_x \tan\alpha_n - s_y\right) \tag{74}$$

and

$$r_{pe,n} \approx \frac{\cos^2\psi_{c,n} \cos^2\alpha_n \left(s_x \tan\alpha_n - s_y\right)^2 - {s_x}^2 - {s_y}^2}{2\left|\mathbf{r}_{c,n}\right|}. \tag{75}$$

Using the identity

$$\cos^2\alpha_n = \frac{1}{1+\tan^2\alpha_n} \tag{76}$$

we note that $r_{pe,n}$ can also be expanded to

$$r_{pe,n} \approx \frac{\cos^2\psi_{c,n} \left(s_x \tan\alpha_n - s_y\right)^2 - {s_x}^2\left(1+\tan^2\alpha_n\right) - {s_y}^2\left(1+\tan^2\alpha_n\right)}{2\left|\mathbf{r}_{c,n}\right|\left(1+\tan^2\alpha_n\right)} \tag{77}$$

or

$$r_{pe,n} \approx \frac{\left({s_x}^2\cos^2\psi_{c,n} - {s_x}^2 - {s_y}^2\right)\tan^2\alpha_n - 2s_y s_x \cos^2\psi_{c,n}\tan\alpha_n + {s_y}^2\left(\cos^2\psi_{c,n} - 1\right)}{2\left|\mathbf{r}_{c,n}\right|\left(1+\tan^2\alpha_n\right)}. \tag{78}$$

Inserting this into the expression for phase error yields

$$\phi_{pe,n} \approx \left\{ \frac{2}{c}\left(\omega_0 + \gamma_0 T_{s,0} i\right) \frac{1}{2\left|\mathbf{r}_{c,n}\right|} \left(\frac{\cos\psi_{c,0}}{\cos\psi_{c,n}}\right) \left(\frac{\left(\begin{array}{l} \left({s_x}^2\cos^2\psi_{c,n} - {s_x}^2 - {s_y}^2\right)\tan^2\alpha_n \\ -2s_y s_x \cos^2\psi_{c,n}\tan\alpha_n \\ +{s_y}^2\left(\cos^2\psi_{c,n} - 1\right) - {s_x}^2 \end{array}\right)}{\left(1+\tan^2\alpha_n\right)\cos\alpha_n} \right) \right\} \tag{79}$$

or

$$\phi_{pe,n} \approx \left\{ \left(\frac{\omega_0 + \gamma_0 T_{s,0} i}{c\left|\mathbf{r}_{c,n}\right|} \right) \left(\frac{\cos\psi_{c,0}}{\cos\psi_{c,n}} \right) \left(\frac{\left(\begin{array}{l} \left(s_x{}^2 \cos^2\psi_{c,n} - s_x{}^2 - s_y{}^2 \right) \tan^2\alpha_n \\ -2 s_y s_x \cos^2\psi_{c,n} \tan\alpha_n \\ + s_y{}^2 \left(\cos^2\psi_{c,n} - 1 \right) - s_x{}^2 \end{array} \right)}{\sqrt{1+\tan^2\alpha_n}} \right) \right\}. \tag{80}$$

For a circular flight path using constant range and constant grazing angle, this can be written as

$$\phi_{pe,n} \approx \left\{ \left(\frac{\omega_0 + \gamma_0 T_{s,0} i}{c\left|\mathbf{r}_{c,0}\right|} \right) \left(\frac{\left(\begin{array}{l} \left(s_x{}^2 \cos^2\psi_{c,n} - s_x{}^2 - s_y{}^2 \right) \tan^2\alpha_n \\ -2 s_y s_x \cos^2\psi_{c,0} \tan\alpha_n \\ + s_y{}^2 \left(\cos^2\psi_{c,0} - 1 \right) - s_x{}^2 \end{array} \right)}{\sqrt{1+\tan^2\alpha_n}} \right) \right\}. \tag{81}$$

Conventional PFA processing will resample data to be linear in $\tan\alpha_n$, consequently we expand this into a series in $\tan\alpha_n$ and write it as

$$\phi_{pe,n} \approx \left\{ \left(\frac{\omega_0 + \gamma_0 T_{s,0} i}{2c\left|\mathbf{r}_{c,0}\right|} \right) \left(\begin{array}{l} + s_y{}^2 2\left(\cos^2\psi_{c,0} - 1 \right) - 2 s_x{}^2 \\ - 4 s_y s_x \cos^2\psi_{c,0} \tan\alpha_n \\ - \left(s_x{}^2 \left(1 - 2\cos^2\psi_{c,n} \right) + s_y{}^2 \left(1 + \cos^2\psi_{c,0} \right) \right) \tan^2\alpha_n \\ + \ldots \end{array} \right) \right\}. \tag{82}$$

We identify the quadratic term as

$$\phi_{qpe,n} \approx \left(\frac{\omega_0 + \gamma_0 T_{s,0} i}{2c\left|\mathbf{r}_{c,0}\right|} \right) \left(- s_x{}^2 \left(1 - 2\cos^2\psi_{c,0} \right) - s_y{}^2 \left(1 + \cos^2\psi_{c,0} \right) \right) \tan^2\alpha_n . \tag{83}$$

Ignoring the dependence on range index *i*, using some conventional simplifications previously identified, yields

$$\phi_{qpe,n} \approx \left(\frac{2\pi}{\lambda_0}\right)\left(\frac{-s_x{}^2\left(1-2\cos^2\psi_{c,0}\right)-s_y{}^2\left(1+\cos^2\psi_{c,0}\right)}{2\left|\mathbf{r}_{c,0}\right|}\right)\tan^2\alpha_n . \tag{84}$$

Effects on focused scene diameter limits

To find maximum scene diameters, we make the substitutions also as previously indicated, with the exception that now, more accurately

$$\tan^2\alpha_n \le \left(\frac{\lambda_0}{4\rho_x\cos\psi_{c,0}}\right)^2 . \tag{85}$$

Consequently,

$$D_x \le 4\rho_x\sqrt{\left(\frac{\left|\mathbf{r}_{c,0}\right|}{\lambda_0}\right)\left(\frac{2\cos^2\psi_{c,0}}{1-2\cos^2\psi_{c,0}}\right)\left(\frac{\phi_{qpe,\max}}{\frac{\pi}{2}}\right)} \tag{86}$$

and

$$D_y \le 4\rho_x\sqrt{\left(\frac{\left|\mathbf{r}_{c,0}\right|}{\lambda_0}\right)\left(\frac{2\cos^2\psi_{c,0}}{1+\cos^2\psi_{c,0}}\right)\left(\frac{\phi_{qpe,\max}}{\frac{\pi}{2}}\right)} . \tag{87}$$

One obvious result of the motion compensation or resampling is to modify the focused scene size limits as a function of grazing angle. We rewrite the scene diameter limits as

$$D_x \le \zeta_x(4\rho_x)\sqrt{\left(\frac{\left|\mathbf{r}_{c,0}\right|}{\lambda_0}\right)\left(\frac{\phi_{qpe,\max}}{\frac{\pi}{2}}\right)} \tag{88}$$

and

$$D_y \le \zeta_y(4\rho_x)\sqrt{\left(\frac{\left|\mathbf{r}_{c,0}\right|}{\lambda_0}\right)\left(\frac{\phi_{qpe,\max}}{\frac{\pi}{2}}\right)} \tag{89}$$

Where the scale factors due to grazing angle are given by

$$\zeta_x = \sqrt{\left(\frac{2\cos^2 \psi_{c,0}}{1 - 2\cos^2 \psi_{c,0}} \right)} \quad = \text{Scene azimuth diameter scale factor, and}$$

$$\zeta_y = \sqrt{\left(\frac{2\cos^2 \psi_{c,0}}{1 + \cos^2 \psi_{c,0}} \right)} \quad = \text{Scene range diameter scale factor.} \qquad (90)$$

These scene diameter scale factors are plotted in Figure 4.

Note that in general the focused scene diameter limits in azimuth are larger than the conventional equation would predict, and the focused scene diameter limits in range are slightly less than the conventional equation would predict.

Example

Consider a Ku-band (16.8 GHz) SAR operating at a 10 km range and 30 degree grazing angle on a circular flight path. The image resolution is 0.1 m on the ground in both dimensions, and is over-sampled by 20%. Allowable peak quadratic phase error is 90 degrees. The focused scene diameter would be 6200 pixels in azimuth by 3300 pixels in range.

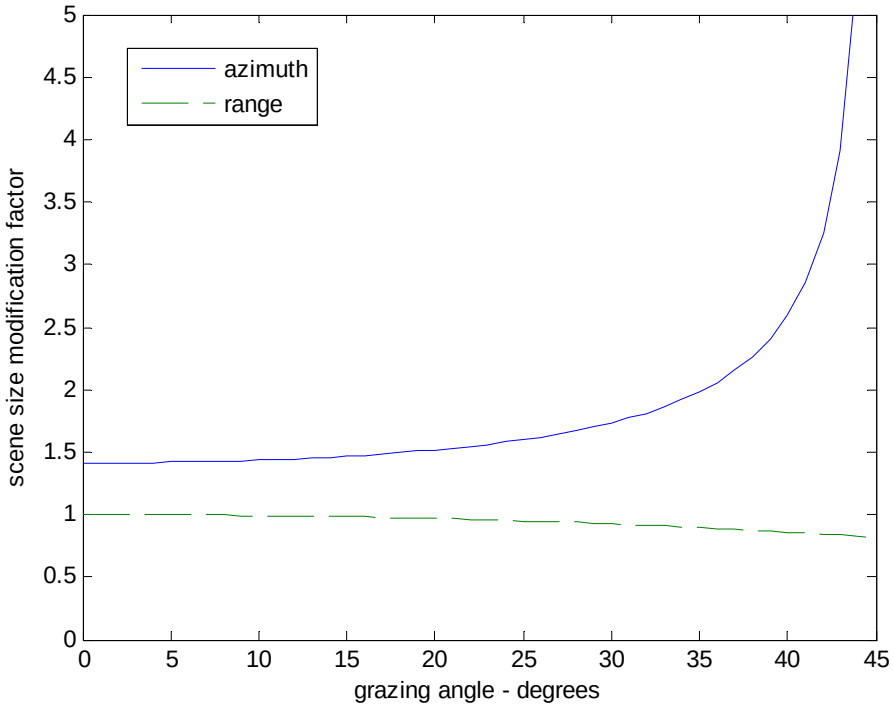

Figure 4. Impact of grazing angle on focused scene diameter for circular flight path.

3.5 Real time motion compensation effects on scene diameter limits – linear flight path at broadside

The previous developments tacitly presumed a circular flight path with constant grazing angle and range. We saw that the grazing angle had a significant impact on focused scene diameter limits. This begs the question "How do the focused scene diameter limits vary with other geometries?"

We explore this by examining another specific radar imaging geometry that is common in SAR operation, namely, level straight-line flight with broadside imaging.

From the previous section we borrow as our starting place the approximate phase error expression

$$\phi_{pe,n} \approx \left\{ \left(\frac{\omega_0 + \gamma_0 T_{s,0} i}{c\left|\mathbf{r}_{c,n}\right|} \right) \left(\frac{\cos\psi_{c,0}}{\cos\psi_{c,n}} \right) \left(\frac{\left(\begin{array}{l} \left(s_x{}^2 \cos^2\psi_{c,n} - s_x{}^2 - s_y{}^2 \right) \tan^2\alpha_n \\ -2 s_y s_x \cos^2\psi_{c,n} \tan\alpha_n \\ + s_y{}^2 \left(\cos^2\psi_{c,n} - 1 \right) - s_x{}^2 \end{array} \right)}{\sqrt{1+\tan^2\alpha_n}} \right) \right\} \tag{91}$$

but now identify that grazing angle and range will vary during the course of the synthetic aperture.

Using the geometry definitions of Figure 3, we identify the radar location vector $\mathbf{r}_{c,n}$ with the 3-tuple $\left(x_{c,n}, y_{c,n}, z_{c,n}\right)$. Straight and level flight that is broadside to the scene center at the aperture center is defined by the relationships

$$\begin{aligned} \tan\alpha_n &= \frac{x_{c,n}}{-y_{c,n}}, \\ \cos\psi_{c,n} &= \left(\frac{\sqrt{x_{c,n}{}^2 + y_{c,n}{}^2}}{\sqrt{x_{c,n}{}^2 + y_{c,n}{}^2 + z_{c,n}{}^2}} \right), \\ \left|\mathbf{r}_{c,n}\right| &= \sqrt{x_{c,n}{}^2 + y_{c,n}{}^2 + z_{c,n}{}^2}, \end{aligned} \tag{92}$$

where

$y_{c,n} = y_{c,0}$, and

$z_{c,n} = z_{c,0}$. (93)

Using these and trig identities, we identify

$$\tan\alpha_n = \frac{x_{c,n}}{-y_{c,0}},$$

$$\cos\alpha_n = \frac{-y_{c,0}}{\sqrt{{x_{c,n}}^2 + {y_{c,0}}^2}} = \frac{1}{\sqrt{1+\tan^2\alpha_n}},$$

$$\cos\psi_{c,n} = \left(\frac{\sqrt{{x_{c,n}}^2 + {y_{c,0}}^2}}{\sqrt{{x_{c,n}}^2 + {y_{c,0}}^2 + {z_{c,0}}^2}}\right) = \left(\frac{\sqrt{1+\tan^2\alpha_n}}{\sqrt{1+\tan^2\psi_{c,0}+\tan^2\alpha_n}}\right),$$

$$\left|\mathbf{r}_{c,n}\right| = \sqrt{{x_{c,n}}^2 + {y_{c,0}}^2 + {z_{c,0}}^2} = \left|\mathbf{r}_{c,0}\right|\cos\psi_{c,0}\sqrt{1+\tan^2\psi_{c,0}+\tan^2\alpha_n}\,. \quad (94)$$

The phase error then becomes

$$\phi_{pe,n} \approx \left\{\left(\frac{\omega_0+\gamma_0 T_{s,0} i}{c}\right)\cos\psi_{c,0}\left(\frac{\left(\begin{array}{l}\left({s_x}^2\left(\frac{1+\tan^2\alpha_n}{1+\tan^2\psi_{c,0}+\tan^2\alpha_n}\right)-{s_x}^2-{s_y}^2\right)\tan^2\alpha_n \\ -2s_y s_x\left(\frac{1+\tan^2\alpha_n}{1+\tan^2\psi_{c,0}+\tan^2\alpha_n}\right)\tan\alpha_n \\ +{s_y}^2\left(\frac{1+\tan^2\alpha_n}{1+\tan^2\psi_{c,0}+\tan^2\alpha_n}-1\right)-{s_x}^2\end{array}\right)}{\left|\mathbf{r}_{c,0}\right|\cos\psi_{c,0}\sqrt{1+\tan^2\alpha_n}\sqrt{1+\tan^2\alpha_n}}\right)\right\} \quad (95)$$

which simplifies to

$$\phi_{pe,n} \approx \left(\frac{\omega_0+\gamma_0 T_{s,0} i}{c\left|\mathbf{r}_{c,0}\right|}\right)\left(\frac{-{s_x}^2-\left({s_x}^2+{s_y}^2\right)\tan^2\psi_{c,0}-2s_y s_x\tan\alpha_n-{s_y}^2\tan^2\alpha_n}{\left(1+\tan^2\psi_{c,0}+\tan^2\alpha_n\right)}\right). \quad (96)$$

For small angles, this can be approximated by the series

$$\phi_{pe,n} \approx \left[\left(\frac{\omega_0 + \gamma_0 T_{s,0} i}{c\left|\mathbf{r}_{c,0}\right|\left(1+\tan^2\psi_{c,0}\right)} \right) \left(\begin{array}{l} -\left(s_x{}^2 + \left(s_x{}^2 + s_y{}^2\right)\tan^2\psi_{c,0}\right) - 2s_y s_x \tan\alpha_n \\ + \left(\dfrac{s_x{}^2 + \left(s_x{}^2 + s_y{}^2\right)\tan^2\psi_{c,0}}{1+\tan^2\psi_{c,0}} - s_y{}^2 \right)\tan^2\alpha_n \\ + \left(\dfrac{2s_y s_x}{1+\tan^2\psi_{c,0}} \right)\tan^3\alpha_n + \left(\dfrac{s_y{}^2}{1+\tan^2\psi_{c,0}} \right)\tan^4\alpha_n \end{array} \right) \right] \tag{97}$$

or

$$\phi_{pe,n} = \left[\left(\frac{\omega_0 + \gamma_0 T_{s,0} i}{c\left|\mathbf{r}_{c,0}\right|\left(1+\tan^2\psi_{c,0}\right)} \right) \left(\begin{array}{l} -\left(s_x{}^2 + \left(s_x{}^2 + s_y{}^2\right)\tan^2\psi_{c,0}\right) - 2s_y s_x \tan\alpha_n \\ + \left(\dfrac{s_x{}^2 - s_y{}^2 + s_x{}^2\tan^2\psi_{c,0}}{1+\tan^2\psi_{c,0}} \right)\tan^2\alpha_n \\ + \left(\dfrac{2s_y s_x}{1+\tan^2\psi_{c,0}} \right)\tan^3\alpha_n + \left(\dfrac{s_y{}^2}{1+\tan^2\psi_{c,0}} \right)\tan^4\alpha_n \end{array} \right) \right]. \tag{98}$$

From this we extract the quadratic term and identify it as

$$\phi_{qpe,n} = \left(\frac{\left(\omega_0 + \gamma_0 T_{s,0} i\right)}{c\left|\mathbf{r}_{c,0}\right|\left(1+\tan^2\psi_{c,0}\right)} \right) \left(\frac{s_x{}^2 - s_y{}^2 + s_x{}^2\tan^2\psi_{c,0}}{1+\tan^2\psi_{c,0}} \right)\tan^2\alpha_n \tag{99}$$

and simplify it to

$$\phi_{qpe,n} = \left(\frac{2\pi}{\lambda_0} \right) \frac{1}{\left|\mathbf{r}_{c,0}\right|} \left(\frac{s_x{}^2}{\left(1+\tan^2\psi_{c,0}\right)} - \frac{s_y{}^2}{\left(1+\tan^2\psi_{c,0}\right)^2} \right)\tan^2\alpha_n \tag{100}$$

and further to

$$\phi_{qpe,n} = \left(\frac{2\pi}{\lambda_0}\right)\frac{\cos^2\psi_{c,0}}{\left|\mathbf{r}_{c,0}\right|}\left(s_x{}^2 - s_y{}^2\cos^2\psi_{c,0}\right)\tan^2\alpha_n\,. \tag{101}$$

By making the same substitutions as in the previous developments, we identify

$$D_x \le 4\rho_x\sqrt{\left(\frac{\left|\mathbf{r}_{c,0}\right|}{\lambda_0}\right)\left(\frac{\phi_{qpe,\max}}{\frac{\pi}{2}}\right)}\,, \tag{102}$$

and

$$D_y \le \frac{4\rho_x}{\cos\psi_{c,0}}\sqrt{\left(\frac{\left|\mathbf{r}_{c,0}\right|}{\lambda_0}\right)\left(\frac{\phi_{qpe,\max}}{\frac{\pi}{2}}\right)}\,. \tag{103}$$

Recognizing that the slant-range scene diameter is

$$D_r = D_y\cos\psi_{c,0} \tag{104}$$

we further identify

$$D_r \le 4\rho_x\sqrt{\left(\frac{\left|\mathbf{r}_{c,0}\right|}{\lambda_0}\right)\left(\frac{\phi_{qpe,\max}}{\frac{\pi}{2}}\right)}\,. \tag{105}$$

The expressions for D_x and D_r are, of course, the classical limits.

We end this section with the comment that Doren,[13] in his dissertation, assumed essentially a linear flight path for his wavefront curvature correction technique.

3.6 Real time motion compensation effects on scene diameter limits – linear flight path with squint

We explore now another specific radar imaging geometry that is common in SAR operation, namely, level straight-line flight with squinted imaging. This will cause additional distortions and defocusing.

As in the previous section we borrow as our starting place the approximate phase error expression

$$\phi_{pe,n} \approx \left\{ \left(\frac{\omega_0 + \gamma_0 T_{s,0} i}{c\left|\mathbf{r}_{c,n}\right|} \right) \left(\frac{\cos\psi_{c,0}}{\cos\psi_{c,n}} \right) \left(\frac{\left(\begin{array}{l} \left(s_x{}^2 \cos^2\psi_{c,n} - s_x{}^2 - s_y{}^2 \right) \tan^2\alpha_n \\ -2 s_y s_x \cos^2\psi_{c,n} \tan\alpha_n \\ + s_y{}^2 \left(\cos^2\psi_{c,n} - 1 \right) - s_x{}^2 \end{array} \right)}{\sqrt{1+\tan^2\alpha_n}} \right) \right\} \tag{106}$$

but now identify that grazing angle and range will vary during the course of the synthetic aperture in a manner consistent with squinted imaging.

Returning again to the geometry definitions of Figure 3, we identify straight and level flight that is squinted to the scene center at the aperture center with the relationships

$$\begin{aligned} \tan\alpha_n &= \frac{x_{c,n}}{-y_{c,n}}, \\ \cos\psi_{c,n} &= \left(\frac{\sqrt{x_{c,n}{}^2 + y_{c,n}{}^2}}{\sqrt{x_{c,n}{}^2 + y_{c,n}{}^2 + z_{c,n}{}^2}} \right), \\ \left|\mathbf{r}_{c,n}\right| &= \sqrt{x_{c,n}{}^2 + y_{c,n}{}^2 + z_{c,n}{}^2}, \end{aligned} \tag{107}$$

where now

$$\begin{aligned} y_{c,n} &= y_{c,0} + x_{c,n} \cot\theta_s, \text{ and} \\ z_{c,n} &= z_{c,0}. \end{aligned} \tag{108}$$

This geometry is illustrated in Figure 5. Note that with $\theta_s = 90$ degrees, this geometry simplifies to the broadside imaging case.

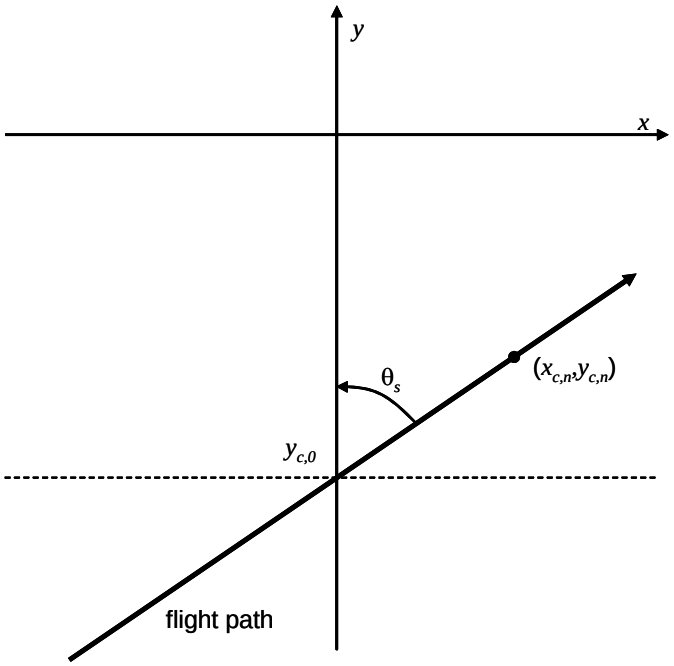

Figure 5. Ground projection of squinted data collection geometry.

Using these and trig identities, we identify

$$\tan\alpha_n = \frac{x_{c,n}}{-\left(y_{c,0} + x_{c,n}\cot\theta_s\right)},$$

$$\cos\psi_{c,n} = \left(\frac{\sqrt{{x_{c,n}}^2 + \left(y_{c,0} + x_{c,n}\cot\theta_s\right)^2}}{\sqrt{{x_{c,n}}^2 + \left(y_{c,0} + x_{c,n}\cot\theta_s\right)^2 + {z_{c,0}}^2}}\right),$$

$$\left|\mathbf{r}_{c,n}\right| = \sqrt{{x_{c,n}}^2 + \left(y_{c,0} + x_{c,n}\cot\theta_s\right)^2 + {z_{c,0}}^2}\,, \tag{109}$$

which can be manipulated to

$$x_{c,n} = \frac{-\,y_{c,0}\,\tan\,\alpha_n}{\left(1+\cot\,\theta_s\,\tan\,\alpha_n\right)},$$

$$\cos\psi_{c,n} = \left(\frac{\sqrt{1+\tan^2\alpha_n}}{\sqrt{1+\tan^2\alpha_n + \tan^2\psi_{c,0}\left(1+\cot\theta_s\tan\alpha_n\right)^2}}\right),$$

$$\left|\mathbf{r}_{c,n}\right| = \frac{\left|\mathbf{r}_{c,0}\right|\cos\psi_{c,0}}{\left(1+\cot\theta_s\tan\alpha_n\right)}\sqrt{1+\tan^2\alpha_n + \tan^2\psi_{c,0}\left(1+\cot\theta_s\tan\alpha_n\right)^2}\,. \tag{110}$$

As before, the phase error then becomes

$$\phi_{pe,n} \approx \left\{ \left(\frac{\omega_0 + \gamma_0 T_{s,0} i}{c} \right) \cos\psi_{c,0} \times \left\{ \frac{\left(\begin{array}{l} \left(s_x{}^2 \left(\frac{1+\tan^2\alpha_n}{1+\tan^2\psi_{c,0}(1+\cot\theta_s\tan\alpha_n)^2+\tan^2\alpha_n} \right) - s_x{}^2 - s_y{}^2 \right) \tan^2\alpha_n \\ -2 s_y s_x \left(\frac{1+\tan^2\alpha_n}{1+\tan^2\psi_{c,0}(1+\cot\theta_s\tan\alpha_n)^2+\tan^2\alpha_n} \right) \tan\alpha_n \\ + s_y{}^2 \left(\frac{1+\tan^2\alpha_n}{1+\tan^2\psi_{c,0}(1+\cot\theta_s\tan\alpha_n)^2+\tan^2\alpha_n} - 1 \right) - s_x{}^2 \end{array} \right)}{\left(\frac{|\mathbf{r}_{c,0}|\cos\psi_{c,0}}{(1+\cot\theta_s\tan\alpha_n)} \right) \sqrt{1+\tan^2\alpha_n}\sqrt{1+\tan^2\alpha_n}} \right\} \right\} \tag{111}$$

which reduces to

$$\phi_{pe,n} \approx \left\{ \left(\frac{\omega_0 + \gamma_0 T_{s,0} i}{c|\mathbf{r}_{c,0}|} \right) \frac{\left(\begin{array}{l} -s_x{}^2 - 2 s_y s_x \tan\alpha_n - s_y{}^2 \tan^2\alpha_n \\ -\left(s_x{}^2 + s_y{}^2\right)\tan^2\psi_{c,0}(1+\cot\theta_s\tan\alpha_n)^2 \end{array} \right)}{\left(\frac{1+\tan^2\psi_{c,0}(1+\cot\theta_s\tan\alpha_n)^2+\tan^2\alpha_n}{1+\cot\theta_s\tan\alpha_n} \right)} \right\}. \tag{112}$$

For small angles, this can be approximated by a series for which the quadratic term can be extracted as

$$\phi_{qpe,n} \approx \left(\frac{2\pi}{\lambda_0} \right) \frac{\cos^2\psi_{c,0}}{|\mathbf{r}_{c,0}|} \left(\begin{array}{l} \left(s_x{}^2 - s_y{}^2\cos^2\psi_{c,0}\right) \\ +2 s_x s_y \left(1-2\cos^2\psi_{c,0}\right)\cot\theta_s \\ +s_y{}^2\left(1-5\cos^2\psi_{c,0}+4\cos^4\psi_{c,0}\right)\cot^2\theta_s \end{array} \right) \tan^2\alpha_n . \tag{113}$$

We will not calculate scene size limits for the squinted case, but calculate an example as indicative of the effects of squint angle on quadratic phase error.

For the case of $\theta_s = 45$ degrees, and $\psi_{c,0} = 45$ degrees, the quadratic phase error is unaffected along the *x*-axis ($s_y = 0$). However, along the *y*-axis ($s_x = 0$), the quadratic phase error doubles from that for the broadside case. This implies a reduced focused scene diameter in the s_y direction.

We end this section with the comment that Doren,[13] in his dissertation, also addressed essentially a squinted linear flight path for his wavefront curvature correction technique.

3.7 PFA Processing Examples

Consider an L-band (1.5 GHz) SAR operating at a 5 km nominal range. The image resolution is 0.3048 m on the ground in both dimensions, and is oversampled by 25%. Figure 6 illustrates the ground truth of point-reflector positions in the scene. Specific reflector targets are pointed out for subsequent reference.

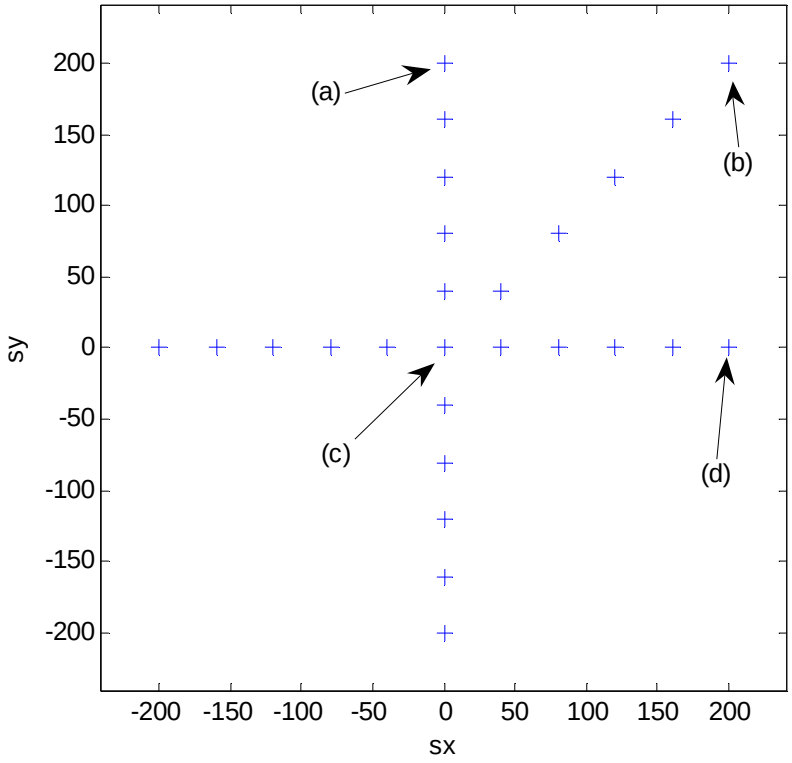

Figure 6. Ground truth for simulated data. Specific reflector targets are called out for subsequent reference.

The conventional limits for focused scene size calculate to approximately 160 m for a peak allowable quadratic phase error of 90 degrees. Targets located at 200 m from the scene center represent a distance 2 ½ times beyond the focused scene edge.

The following plots show the results of conventional PFA processing on target Impulse Response (IPR) with data collected at various imaging geometries.

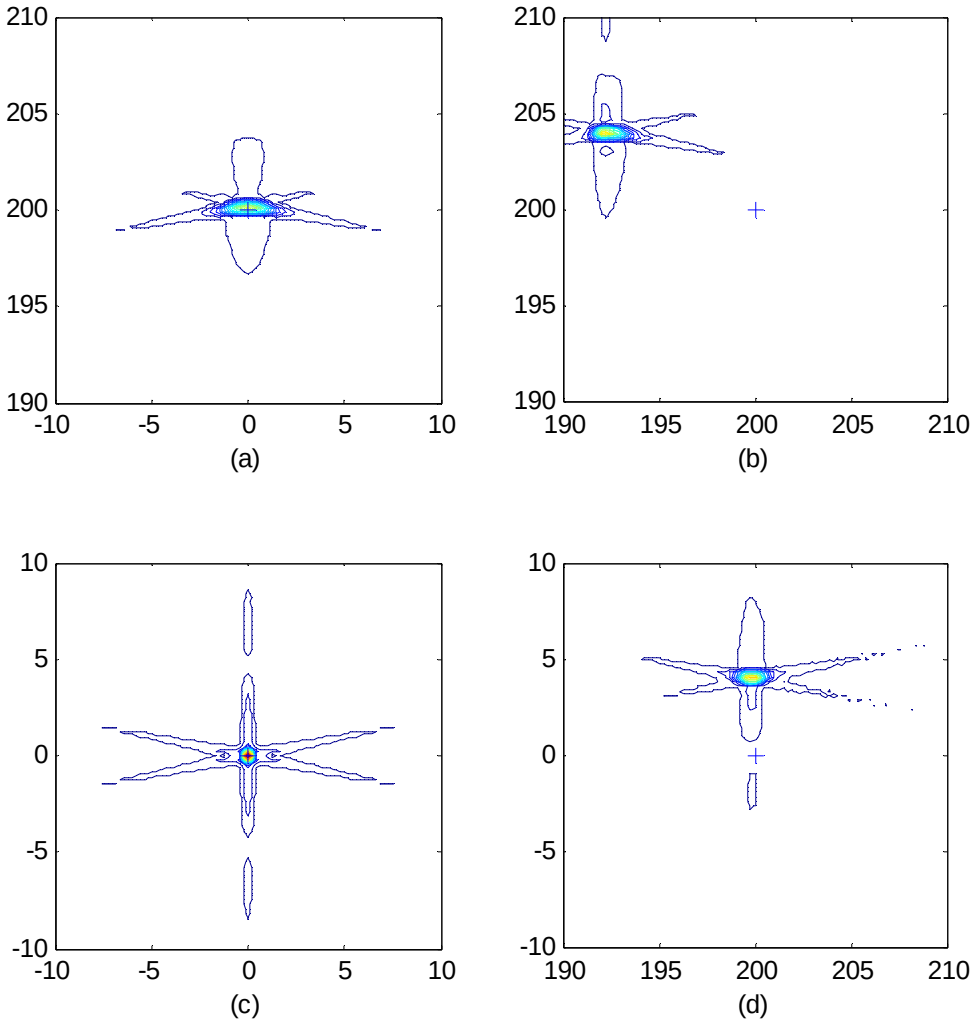

Figure 7. Contour plots of selected targets. Labels correspond to positions in Figure 6. Data was collected from a circular flight path at a 10 degrees grazing angle. Image was processed using PFA processing employing a –35 dB Taylor window in range and azimuth.

Displacements from the "+" symbol represents geometric distortion or warping of the image. Broadening of the IPR is due to defocusing. The forked nature of the azimuth sidelobes are due to the trapezoidal aperture in the Fourier space of the target scene.

Note that the scene center (c) is well focused, but targets displaced at (a), (b), and (d) suffer substantial blurring.

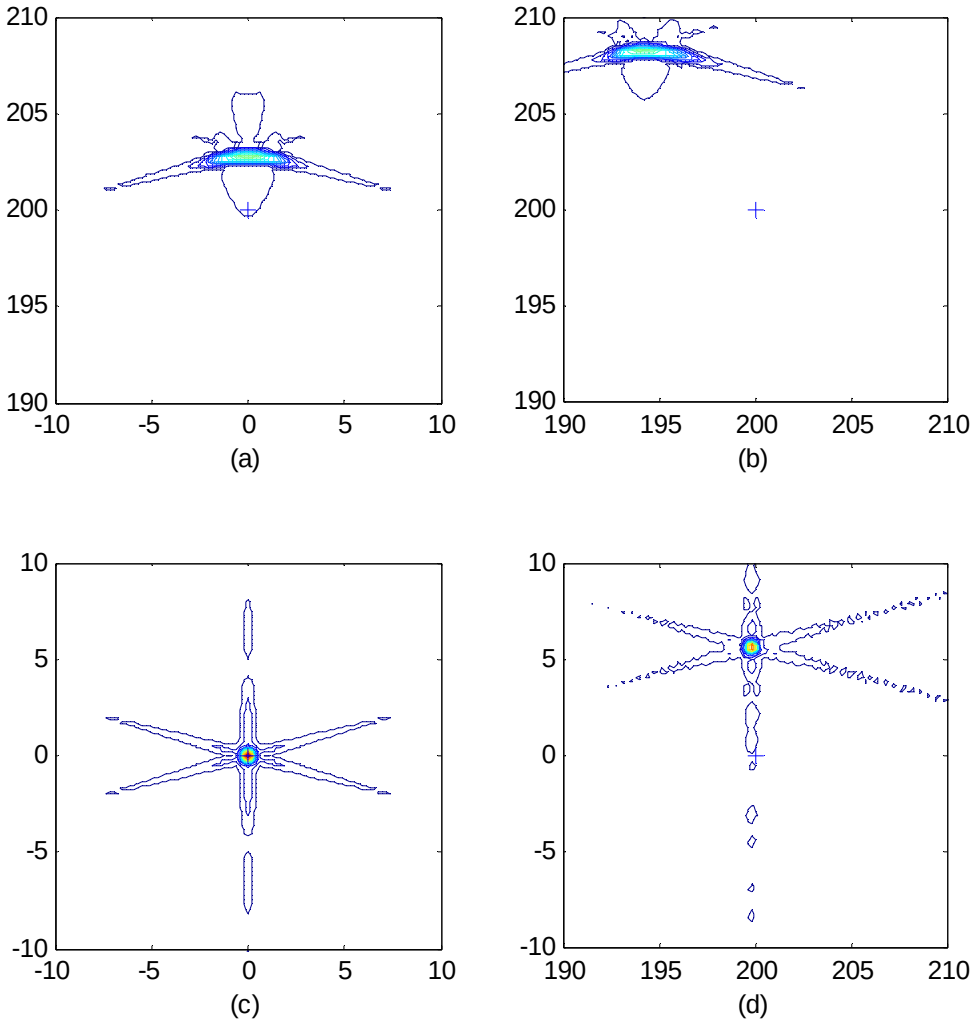

Figure 8. Contour plots of selected targets. Labels correspond to positions in Figure 6. Data was collected from a circular flight path at a 45 degrees grazing angle. Image was processed using PFA processing employing a –35 dB Taylor window in range and azimuth.

Note that the scene center (c) is well focused, but compared to Figure 7, the target displaced at (d) also exhibits nearly ideal focus. However, the targets at (a) and (b) now exhibit substantially degraded focusing. Merely changing the otherwise constant grazing angle has degraded some targets and improved others.

Fortunately, that the target at (d) remains well focused is predicted by the analysis of real-time motion compensation effects on PFA focused scene diameter.

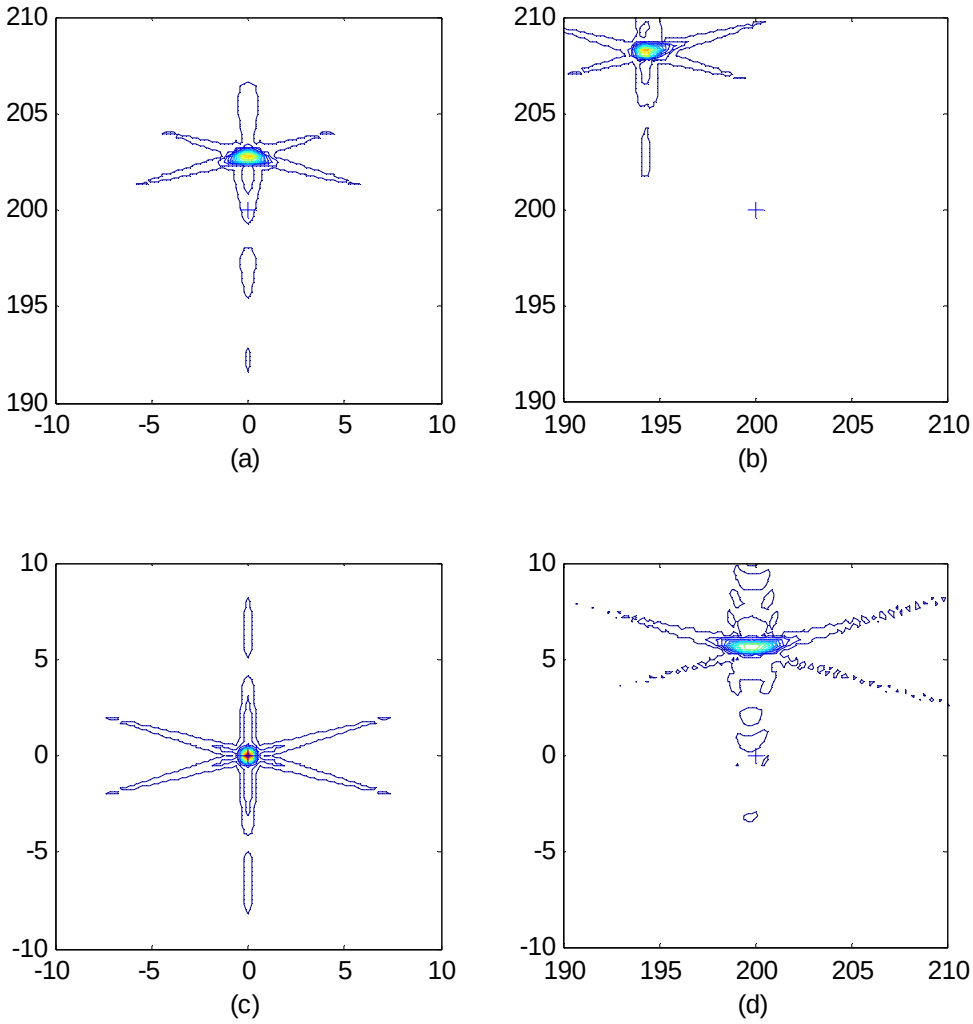

Figure 9. Contour plots of selected targets. Labels correspond to positions in Figure 6. Data was collected from a linear broadside flight path at a nominal 45 degrees grazing angle. Image was processed using PFA processing employing a –35 dB Taylor window in range and azimuth.

Note that the scene center (c) is well focused, but compared to Figure 8, the target displaced at (d) now suffers severe blurring. Targets at (a) and (b) are improved, but still substantially blurred.

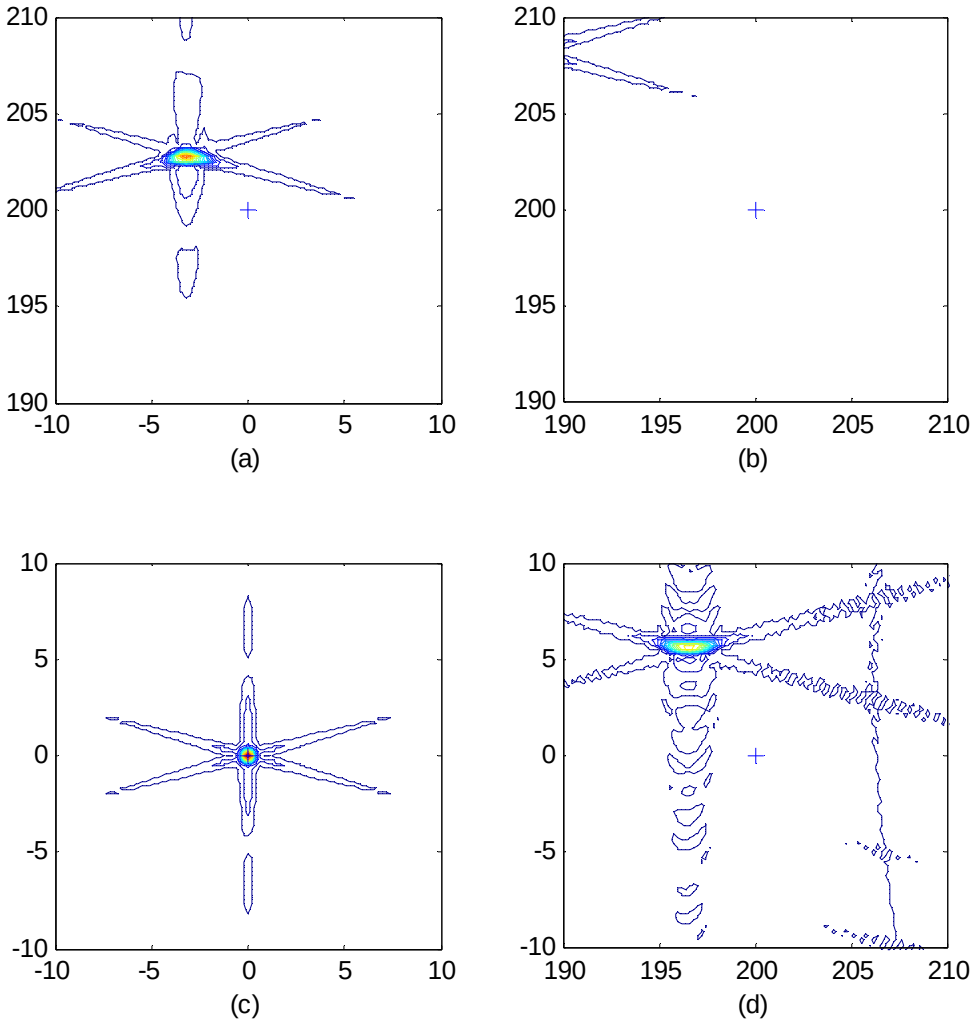

Figure 10. Contour plots of selected targets. Labels correspond to positions in Figure 6. Data was collected from a linear squinted flight path at a nominal 45 degrees grazing angle and 60 degree squint angle (30 degrees forward of broadside). Image was processed using PFA processing employing a –35 dB Taylor window in range and azimuth.

Note that the scene center (c) remains well focused, but compared to Figure 8, the remaining targets exhibit similar blurring, but now suffer additional displacement.

The message here is that even in a perfectly formed PFA processed image, the nature of wavefront curvature effects is very imaging geometry dependent, as one might expect, especially with the clarity of hindsight. Consequently, one might expect that any mitigation scheme also be imaging geometry dependent.

3.8 Wavefront Curvature Correction

Recall that after RVPE compensation, the residual phase error is

$$\phi_{pe,n} = \frac{2}{c}\left(\omega_0 + \gamma_0 T_{s,0} i\right)\kappa_n \left(\left|\mathbf{r}_{c,n}\right| \left(1 - \sqrt{1 - \frac{2\mathbf{n}_{c,n} \bullet \mathbf{s}}{\left|\mathbf{r}_{c,n}\right|} + \frac{\left|\mathbf{s}\right|^2}{\left|\mathbf{r}_{c,n}\right|^2}} \right) - \left(\mathbf{n}_{c,n} \bullet \mathbf{s}\right) \right). \tag{114}$$

Recall also that a reasonable approximation for the dominant characteristic of the phase error is

$$\phi_{pe,n} \approx \frac{2}{c}\left(\omega_0 + \gamma_0 T_{s,0} i\right)\kappa_n \left(\frac{\left(\mathbf{n}_{c,n} \bullet \mathbf{s}\right)^2 - \left|\mathbf{s}\right|^2}{2\left|\mathbf{r}_{c,n}\right|} \right). \tag{115}$$

Incorporating real-time motion compensation (or an equivalent range interpolation) allowed us to describe the dominant error as

$$\phi_{pe,n} \approx \left\{ \left(\frac{\omega_0 + \gamma_0 T_{s,0} i}{c\left|\mathbf{r}_{c,n}\right|} \right) \left(\frac{\cos\psi_{c,0}}{\cos\psi_{c,n}} \right) \left(\frac{\left(\begin{array}{l} \left(s_x{}^2 \cos^2\psi_{c,n} - s_x{}^2 - s_y{}^2\right)\tan^2\alpha_n \\ -2 s_y s_x \cos^2\psi_{c,n} \tan\alpha_n \\ + s_y{}^2\left(\cos^2\psi_{c,n} - 1\right) - s_x{}^2 \end{array} \right)}{\sqrt{1+\tan^2\alpha_n}} \right) \right\}. \tag{116}$$

To explore the characteristics of this further, we again presume for the moment a circular flight path, and recall the phase error for this as approximated by the series

$$\phi_{pe,n} \approx \left\{ \left(\frac{\omega_0 + \gamma_0 T_{s,0} i}{2c\left|\mathbf{r}_{c,0}\right|} \right) \left[\begin{array}{l} s_y{}^2 2\left(\cos^2\psi_{c,0} - 1\right) - 2 s_x{}^2 \\ -4 s_y s_x \cos^2\psi_{c,0} \tan\alpha_n \\ -\left(s_x{}^2\left(1 - 2\cos^2\psi_{c,n}\right) + s_y{}^2\left(1 + \cos^2\psi_{c,0}\right)\right)\tan^2\alpha_n \\ + \ldots \end{array} \right] \right\}. \tag{117}$$

Some comments are in order.

- Within the square brackets, the first and second terms are responsible for a spatially variant shift, that it, a geometric distortion in the image. This is most

noticeable in large images with long linear features such as roads not appearing straight in spite of ground-truth indicating straightness.

- The third term in the square brackets is quadratic in $\tan\alpha_n$ and represents a quadratic phase error that defocuses the image in a spatially variant manner. Compensating only this term will substantially enhance focusing at points distant from the scene center, although not address geometric distortions of the other terms.

- The quadratic term does exhibit a relatively weak dependence in range index *i*, which can usually be ignored for all but the finest resolutions where chirp bandwidth becomes a large fraction of the radar center frequency.

- For this geometry, the quadratic term exhibits a significant dependence on grazing angle. As $\psi_{c,0}$ approaches 45 degrees, the dependence on azimuth position s_x disappears. This is a consequence of the circular flight path and range interpolation (which can be implemented via real-time motion compensation) and also including more terms in the phase error approximation. This is not fully appreciated in earlier discussions of this technique. Ignoring this will result in over-correcting for an error, that may in fact generate a larger quadratic error than originally existed.

- A tacit assumption is that $\tan\alpha_n$ is linear in azimuth data index *n*. This is justified because the azimuth resampling involved in PFA processing will in fact force this relationship for any index *i*, although the constant of proportionality will depend on the specific index *i*.

Correcting for wavefront curvature effects

Correcting for wavefront curvature effects requires compensation for the phase error terms that cause the problematic effects. However, the effects, and the phase errors that cause them are spatially variant, that is, they are different in different parts of the scene.

The basic procedure is to use a deconvolution that is adjusted for different parts of the image based on the expected degrading phase error function for that neighborhood in the image. This is illustrated in Figure 11 and Figure 12. The deconvolution is implemented as a convolution with the DFT of the conjugate of the phase error.

The convolution kernel for subimage *f* is given by

$$\exp\left\{-j\phi_{pe,n}\right\}\Big|_{\substack{s_x=s_{x,f}\\ s_y=s_{y,f}}} \tag{118}$$

For whatever aspect of the phase error needs to be corrected.

Recall, however, that the phase error expressions were quite different depending on the flight path. So, too, will be the correction operation.

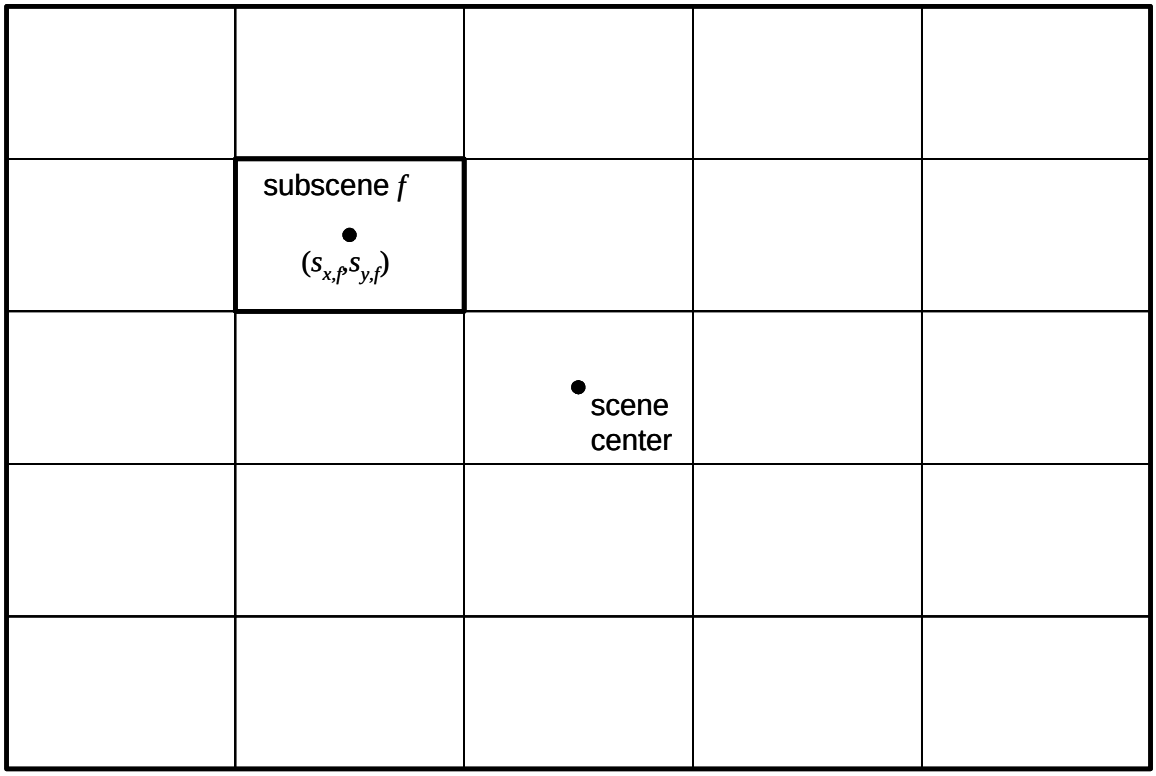

Figure 11. Illustration of subimages within total image. Each subimage is focused by deconvolving the entire subimage with the expected phase error at the subimage center.

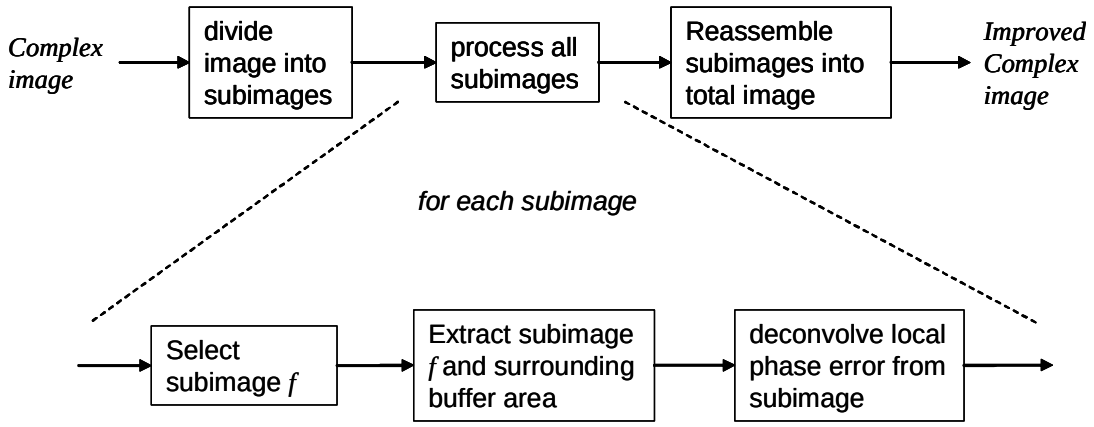

Figure 12. Processing steps for wavefront curvature correction.

Some comments are in order.

- Of course, the convolution can be implemented as fast convolution using DFTs and Inverse DFTs.
- The subimage size can be as little as a single pixel in either or both dimensions, but needs to be less than a size with acceptable residual blurring.
- Larger subimage sizes will allow more efficiency in processing.
- Larger subimage sizes will allow greater phase function discontinuities at subimage boundaries.

Since the specific correction is flight path dependent, we begin with a generalization of the phase error that is also not flight path dependent. We once again identify a generic approximation

$$\phi_{pe,n} \approx \left\{ \left(\frac{\omega_0 + \gamma_0 T_{s,0} i}{c} \right) \cos\psi_{c,0} \left[\frac{\left(\begin{array}{l} \left({s_x}^2 \cos^2\psi_{c,n} - {s_x}^2 - {s_y}^2 \right) \tan^2\alpha_n \\ -2 s_y s_x \cos^2\psi_{c,n} \tan\alpha_n \\ + {s_y}^2 \left(\cos^2\psi_{c,n} - 1 \right) - {s_x}^2 \end{array} \right)}{\left| \mathbf{r}_{c,n} \right| \cos\psi_{c,n} \sqrt{1 + \tan^2\alpha_n}} \right] \right\} \tag{119}$$

where flight-path dependent terms have been combined inside the square brackets.

With a specific flight path, this can be written in a series form

$$\phi_{pe,n} \approx \left\{ \left(\frac{\omega_0 + \gamma_0 T_{s,0} i}{c} \right) \cos\psi_{c,0} \left[\varphi(0) + \frac{d\varphi(0)}{d\tan\alpha_n} \tan\alpha_n + \left(\frac{1}{2} \right) \frac{d^2\varphi(0)}{d\tan^2\alpha_n} \tan^2\alpha_n + \ldots \right] \right\} \tag{120}$$

where

$$\varphi(\tan\alpha_n) = \frac{\left(\begin{array}{l} \left({s_x}^2 \cos^2\psi_{c,n} - {s_x}^2 - {s_y}^2 \right) \tan^2\alpha_n \\ -2 s_y s_x \cos^2\psi_{c,n} \tan\alpha_n \\ + {s_y}^2 \left(\cos^2\psi_{c,n} - 1 \right) - {s_x}^2 \end{array} \right)}{\left| \mathbf{r}_{c,n} \right| \cos\psi_{c,n} \sqrt{1 + \tan^2\alpha_n}} \tag{121}$$

and recognizing that $\left|\mathbf{r}_{c,n}\right|$ and $\psi_{c,n}$ are both also generally functions of $\tan\alpha_n$ in a manner defined by the specific flight path.

Wavefront curvature effects may be corrected in part or in whole. This is accomplished by selecting which error terms of the expansion are intolerable in the final image.

Furthermore, wavefront curvature effects may be corrected in pieces, that is, defocusing may be corrected in separate operations from warping. In fact, the correction of each piece may occur over a different division of subimages.

Correcting for defocusing due to wavefront curvature

The most basic operation is to merely correct the focus of the image, and ignore spatial distortions. We may then presume the significant portion of the phase error to be the quadratic term, or

$$\phi_{qpe,n} \approx \left\{\left(\frac{\omega_0}{c}\right)\cos\psi_{c,0}\left[\left(\frac{1}{2}\right)\frac{d^2\varphi(0)}{d\tan^2\alpha_n}\tan^2\alpha_n\right]\right\}. \tag{122}$$

Figure 13 has only this element of the wavefront curvature phase error correction applied. Note that focusing has improved, but the position offset remains.

Correcting for azimuth shifting due to wavefront curvature

The principal component contributing to azimuth shifting is the linear term

$$\phi_{pe,n} \approx \left\{\left(\frac{\omega_0}{c}\right)\cos\psi_{c,0}\left[\frac{d\varphi(0)}{d\tan\alpha_n}\tan\alpha_n\right]\right\}. \tag{123}$$

Figure 14 illustrates the addition of this element of the wavefront curvature phase error correction to that illustrated in Figure 13. Note how its position in the *x*-direction is improved.

Correcting for range shifting due to wavefront curvature

The principle component contributing to range shifting is the term linear in index *i*, namely

$$\phi_{pe,n} \approx \left\{\left(\frac{\gamma_0 T_{s,0} i}{c}\right)\cos\psi_{c,0}\left[\varphi(0)\right]\right\}. \tag{124}$$

Figure 15 illustrates the addition of this element of the wavefront curvature phase error correction to that illustrated in Figure 14. Note how its position in the *y*-direction is now improved.

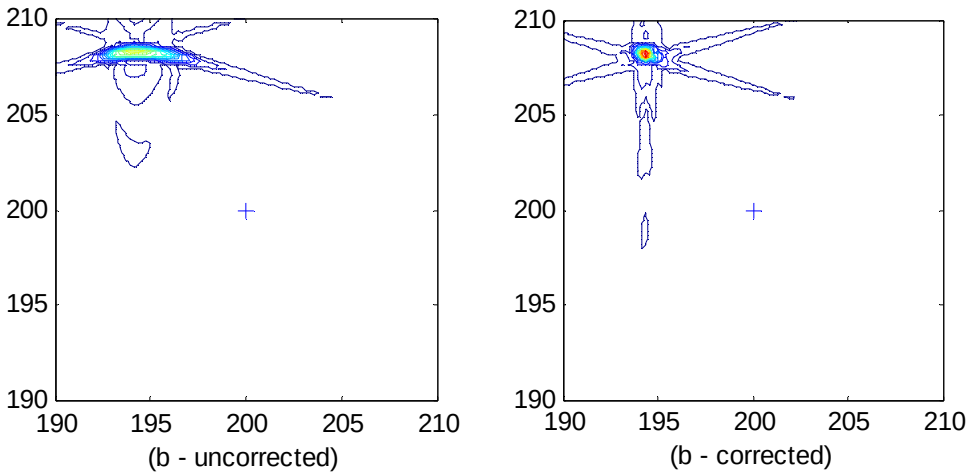

Figure 13. Contour plots of selected target before and after wavefront curvature correction. Correction was for focusing only. Data was collected from a circular flight path at a 45 degrees grazing angle, identical to Figure 8. Image was processed using PFA processing employing a –35 dB Taylor window in range and azimuth.

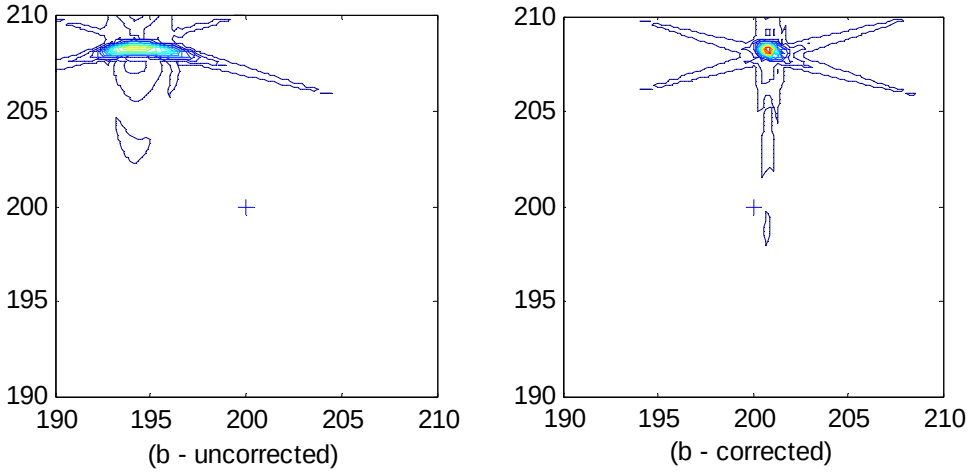

Figure 14. Contour plots of selected target before and after wavefront curvature correction. Correction included focusing and azimuth displacements. Data was collected from a circular flight path at a 45 degrees grazing angle, identical to Figure 8. Image was processed using PFA processing employing a –35 dB Taylor window in range and azimuth.

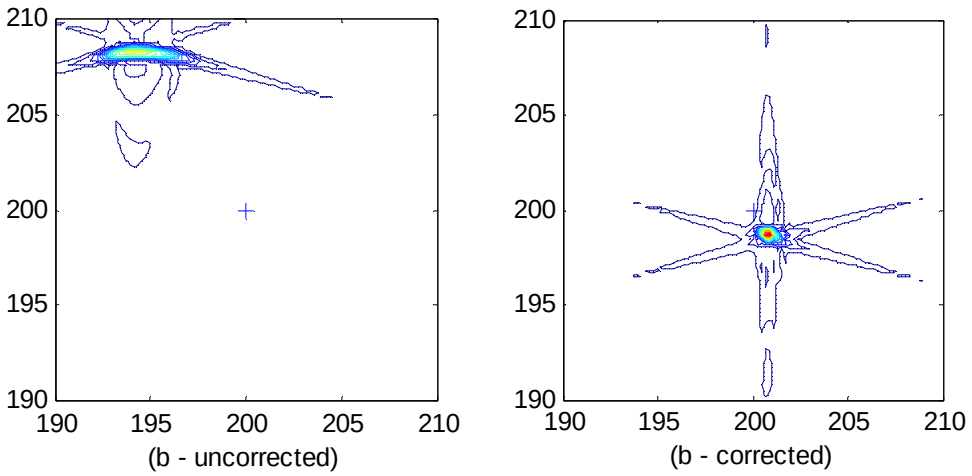

Figure 15. Contour plots of selected target before and after wavefront curvature correction. Correction included focusing and azimuth and range displacements. Data was collected from a circular flight path at a 45 degrees grazing angle, identical to Figure 8. Image was processed using PFA processing employing a –35 dB Taylor window in range and azimuth.

Scene diameter limits

With the image divided into subimages, let

$$k_{subimages,x} = \text{number of subimages per row, and}$$
$$k_{subimages,y} = \text{number of subimages per column.} \tag{125}$$

Since each subimage is now focused at its own center, each subimage now enjoys the scene size limits of the former uncompensated entire image. Consequently, to first order, the overall scene diameter limits have been extended by the number of subimages per row, or column, as warranted. That is,

$$D_{x,compensated} \le k_{subimages,x} D_{x,uncompensated} \text{ , and}$$
$$D_{y,compensated} \le k_{subimages,y} D_{y,uncompensated} \text{ .} \tag{126}$$

For the classical limits,

$$D_{x,compensated} \le k_{subimages,x} (4\rho_x) \sqrt{\left(\frac{|\mathbf{r}_{c,0}|}{\lambda_0}\right)\left(\frac{\phi_{qpe,\max}}{\pi/2}\right)},$$
$$D_{y,compensated} \le k_{subimages,y} (4\rho_x) \sqrt{\left(\frac{|\mathbf{r}_{c,0}|}{\lambda_0}\right)\left(\frac{\phi_{pe,\max}}{\pi/2}\right)}. \tag{127}$$

3.9 Wavefront Curvature Correction Examples

The following plots show the results of applying wavefront curvature correction to the images of Figure 7 through Figure 10.

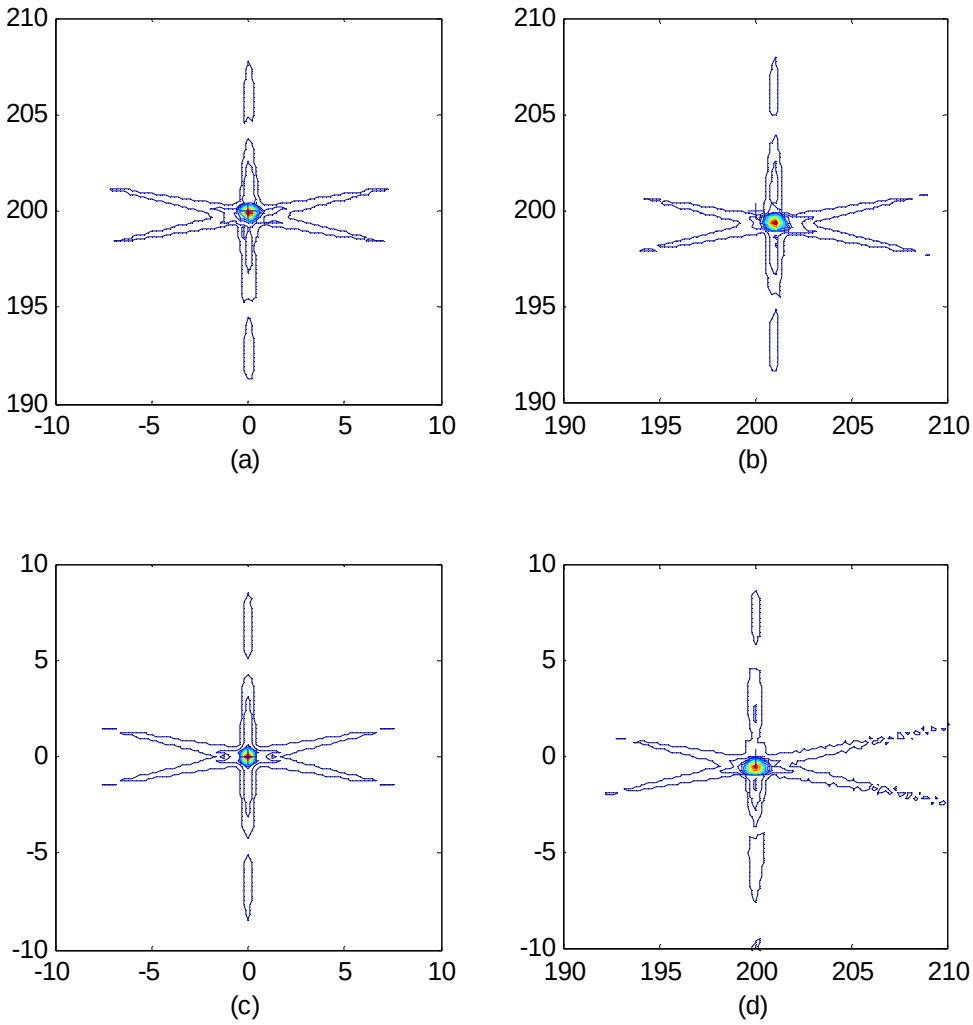

Figure 16. Results of Wavefront Curvature correction applied via post processing to image of Figure 7 formed from data collected from a circular flight path. Images are corrected for defocus as well as azimuth shifting and range shifting. The original image was divided into a grid of 7 x 7 subimages.

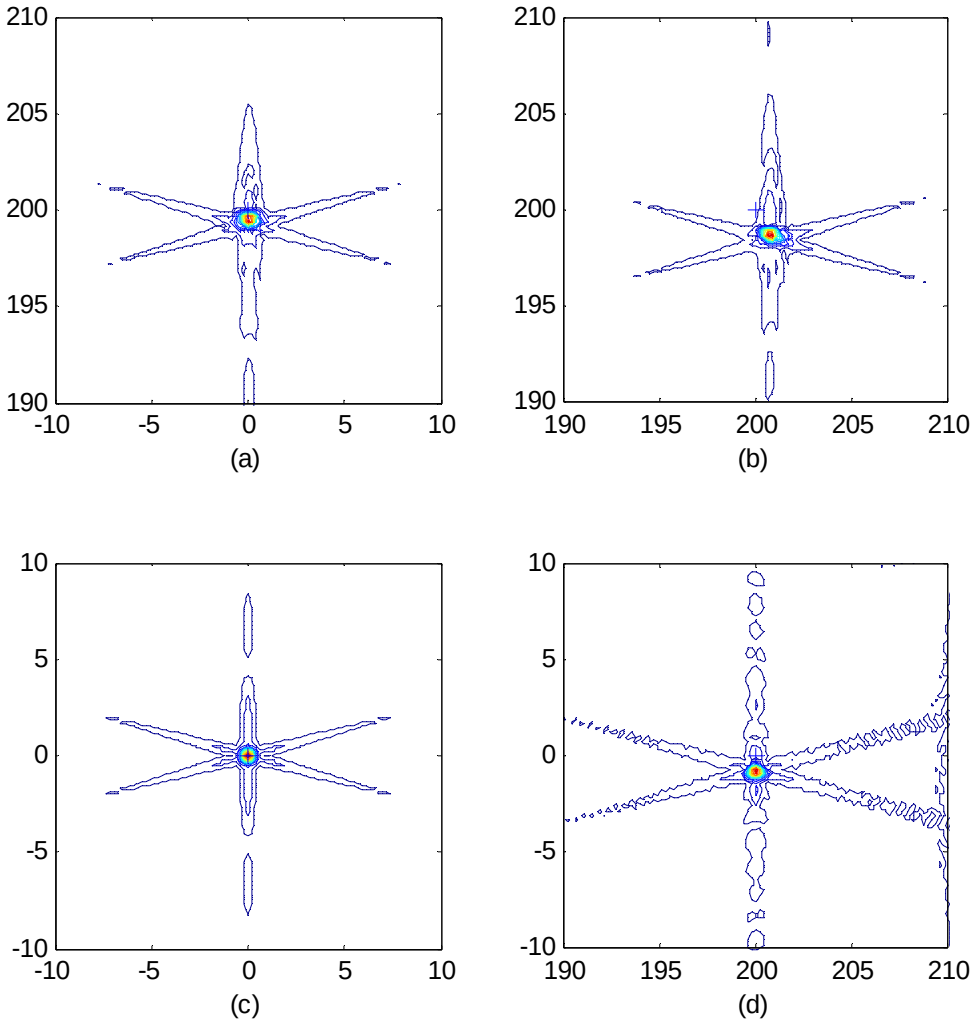

Figure 17. Results of Wavefront Curvature correction applied via post processing to image of Figure 8 formed from data collected from a circular flight path. Images are corrected for defocus as well as azimuth shifting and range shifting. The original image was divided into a grid of 7 x 7 subimages.

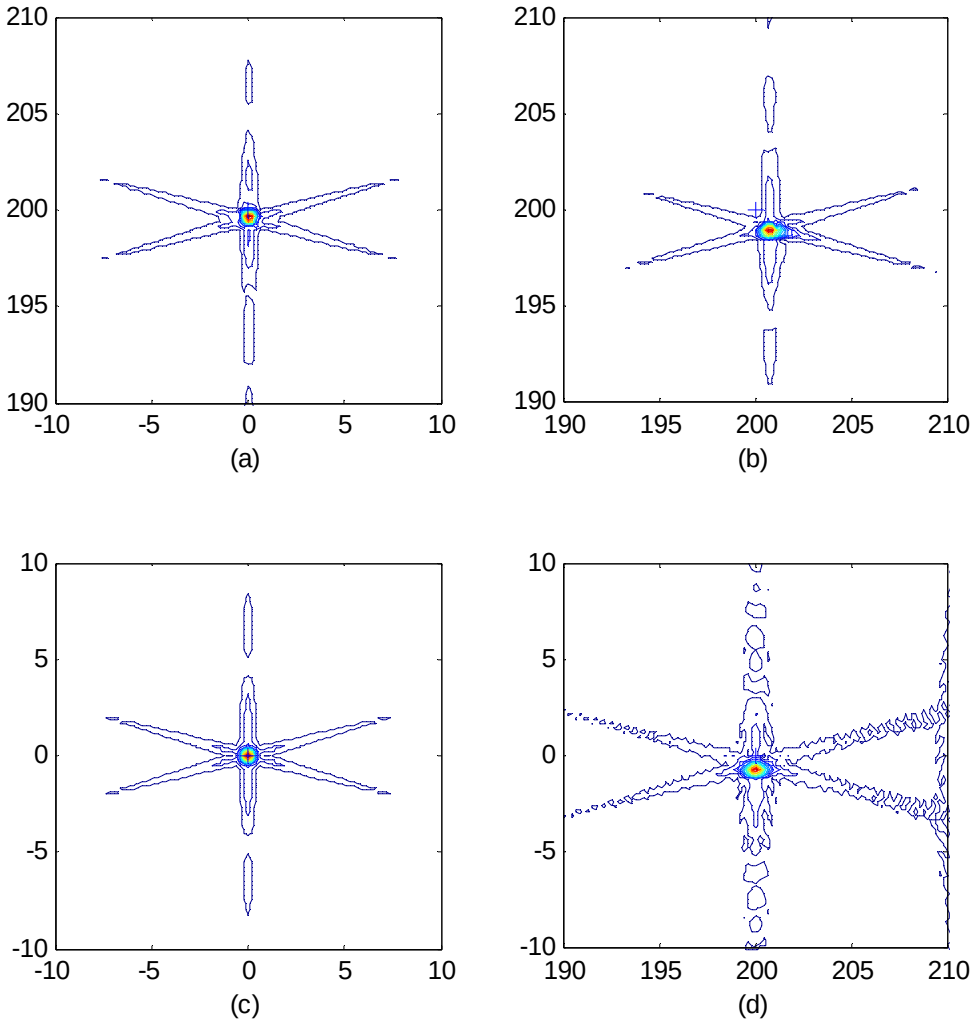

Figure 18. Results of Wavefront Curvature correction applied via post processing to image of Figure 9 formed from data collected from a broadside linear flight path. Images are corrected for defocus as well as azimuth shifting and range shifting. The original image was divided into a grid of 7 x 7 subimages.

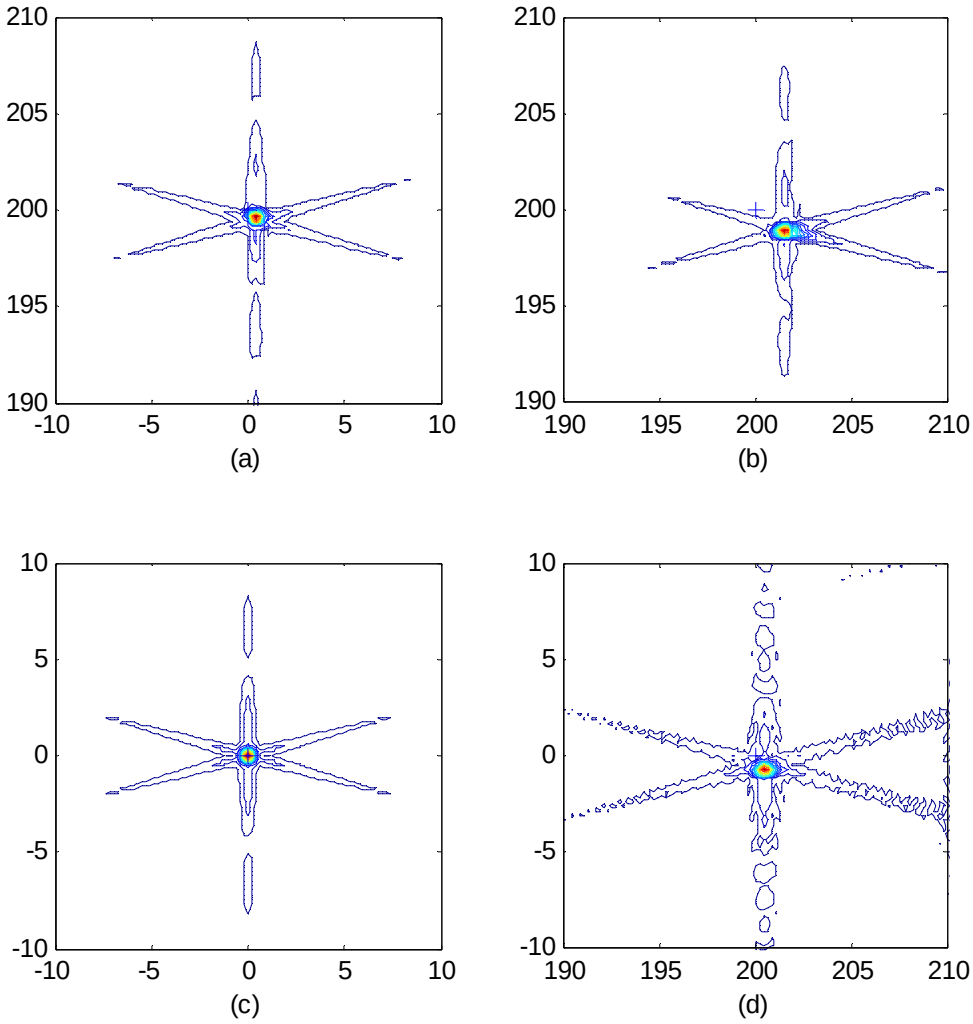

Figure 19. Results of Wavefront Curvature correction applied to squinted image of Figure 10 via post processing. Images are corrected for defocus as well as azimuth shifting and range shifting. The original image was divided into a grid of 7 x 7 subimages.

3.10 Relationship to subaperture processing

It is noteworthy that the subimage processing discussed in the previous sections is very related to subaperture processing.

In fact the coarse-resolution pixels from subaperture processing are related by a transform to subimages in the final image.

Consequently, subimages can be treated as the DFT of equivalent coarse-resolution pixels derived from subaperture processing.

Furthermore, deconvolution (or convolution) that is subimage dependent is equivalent to multiplication (including by phase correction vectors) across a set of like coarse resolution pixels derived from subapertures.

As such, subimage processing and subaperture processing are in a gross sense mathematically equivalent. Differences are more a matter of implementation.

3.11 Comments on stripmap imaging

In modern high-performance SAR systems, stripmap images are typically formed by mosaicking individual SAR image patches to create a seamless larger image strip. Individual image patches are formed by spotlight SAR imaging techniques.

PFA is inherently a spotlight SAR imaging technique. Stripmap imaging with PFA is done by this mosaicking technique. Imaging geometry is typically straight-line flight path with broadside (non-squinted) imaging.

To form a seamless stripmap from successive non-overlapping synthetic apertures, we require that the focused image azimuth diameter be larger than the synthetic aperture is long. That is

$$D_{x,compensated} \geq L_{ap} \tag{128}$$

where

$$L_{ap} = \frac{\lambda_0 \left| \mathbf{r}_{c,0} \right|}{2\rho_x} \ . \tag{129}$$

From this we calculate the minimum number of subimages per row as

$$k_{subimages,x} \geq \frac{\lambda_0^{3/2} \sqrt{\left| \mathbf{r}_{c,0} \right|}}{8\rho_x^{\,2} \sqrt{\frac{\phi_{qpe,\max}}{\pi/2}}} . \tag{130}$$

Example

Consider a Ku-band (16.8 GHz) SAR operating in stripmap mode at 5 km range. The focused image resolution is required to be 0.1 m on the ground in both dimensions. Allowable residual quadratic phase error is 45 degrees.

The minimum number of subimages per row is calculated and rounded up to three. If we allow for a window function broadening factor of $a_{w,x} = 1.2$, then this increases to 5.

Example

Consider the L-band examples of section 3.7, where frequency was 1.5 GHz, at a range of 5 km and at 0.3048 m resolution. Let us allow a residual quadratic phase error of 90 degrees.

The minimum number of subimages per row is calculated and rounded up to 9. If we allow for a window function broadening factor of $a_{w,x} = 1.2$, then this increases to 13.

4 Conclusions

The following principal conclusions should be drawn from this report.

- PFA processing scene diameter limits are defined by allowable blurring at the scene edges by a residual quadratic phase error.
- The residual quadratic phase error is spatially variant.
- The nature of the residual phase error depends on the specific flight path used to collect the raw phase history data.
- The residual quadratic phase error is deterministic.
- The residual quadratic phase error can be corrected by a spatially variant phase error correction filtering operation.
- The spatially variant phase error correction is also flight path dependant.
- The basic correction scheme is to divide the image into subimages, and compensate each subimage according to its location in the overall image.
- Correcting the image spatially variant phase errors in this manner allows a considerable increase in the focused scene diameter of a PFA processed image.
- Image geometric distortion can also be corrected in this manner.
- Subimage processing schemes are very related to subaperture processing schemes.

The novelty within this report is the extension of wavefront curvature correction to an arbitrary imaging geometry (flight path).

Matlab files used

pfascene.m
generate.m
gentarg.m
genparm.m
genpath.m
genphas.m
genimage.m
minisar_pf_v11.m
gendisp.m
wc_correct.m

REFERENCES

[1] J. L. Walker, “Range-Doppler Imaging of Rotating Objects,” IEEE Trans. on Aerospace and Electronic Systems, AES-16 (1), pp 23-52, (1980).

[2] Walter G. Carrara, Ron S. Goodman, Ronald M. Majewski, *Spotlight Synthetic Aperture Radar, Signal Processing Algorithms*, ISBN 0-89006-728-7, Artech House Publishers, 1995.

[3] C. V. Jakowatz Jr., D. E. Wahl, P. H. Eichel, D. C. Ghiglia, P. A. Thompson, *Spotlight-Mode Synthetic Aperture Radar: A Signal Processing Approach*, ISBN 0-7923-9677-4, Kluwer Academic Publishers, 1996.

[4] Grant D. Martin, Armin W. Doerry, Michael W. Holzrichter, “A Novel Polar Format Algorithm for SAR Images Utilizing Post Azimuth Transform Interpolation”, Sandia Report SAND2005-5510, September 2005.

[5] Grant D. Martin, Armin W. Doerry, “SAR Polar Format Implementation with MATLAB”, Sandia Report SAND2005-7413, Unlimited Release, November 2005.

[6] Armin W.Doerry, “Real-time Polar-Format Processing for Sandia’s Testbed Radar Systems”, Sandia Internal Memorandum SAND2001-1644P, Internal Distribution Only, June 2001.

[7] A. W. Doerry, “Patch Diameter Limitation due to High Chirp Rates in Focused SAR Images”, IEEE Transactions on Aerospace and Electronic Systems, Vol. 30, No. 4, October 1994.

[8] A. W. Doerry, "Synthetic Aperture Radar Processing with Polar Formatted Subapertures", Conference Record of The Twenty-Eighth Asilomar Conference on Signals, Systems & Computers, pp 1210-1215, Pacific Grove, California, Oct. 31 - Nov. 2, 1994.

[9] Armin W. Doerry, "Synthetic Aperture Radar Processing with Tiered Subapertures", Ph.D. Dissertation, University of New Mexico, Albuquerque, New Mexico, May, 1995.

[10] Armin W.Doerry, "Synthetic Aperture Radar Processing with Tiered Subapertures", Sandia Report SAND94-1390, June, 1994.

[11] N. E. Doren, C.V. Jakowatz, Jr., D.E. Wahl, P.A.Thompson, “General formulation for wavefront curvature correction in polar-formatted spotlight-mode SAR images

using space-variant post-filtering", Proceedings., 1997 International Conference on Image Processing, Vol. 1, pp 861–864, 26-29 Oct. 1997.

[12] C. V. Jakowatz, D. E. Wahl, P. A. Thompson, N. E. Doren, "Space-variant filtering for correction of wavefront curvature effects in spotlight-mode SAR imagery formed via polar formatting", Proceedings of the SPIE - The International Society for Optical Engineering, Algorithms for Synthetic Aperture Radar Imagery IV, vol. 3070, pp 33-42, Orlando, FL, USA, Apr 23-24, 1997.

[13] Neall E. Doren, "Space-Variant Post-Filtering for Wavefront Curvature Correction in Polar-Formatted Spotlight-Mode SAR Imagery", Sandia Report SAND99-2706, Unlimited Release, October 1999.

“Few things are harder to put up with than the annoyance of a good example.”

Mark Twain

DISTRIBUTION

Unlimited Release

1	MS 1330	S. C. Holswade	5340
1	MS 1330	B. L. Burns	5340
1	MS 1330	W. H. Hensley	5342
1	MS 1330	T. P. Bielek	5342
1	MS 1330	A. W. Doerry	5342
1	MS 1330	D. Harmony	5342
1	MS 1330	S. S. Kawka	5342
1	MS 1330	M. S. Murray	5342
1	MS 1330	D. G. Thompson	5342
1	MS 1330	K. W. Sorensen	5345
1	MS 1330	D. F. Dubbert	5345
1	MS 1330	G. R. Sloan	5345
1	MS 1330	S. M. Becker	5348
1	MS 1330	M. W. Holzrichter	5348
1	MS 1330	O. M. Jeromin	5348
1	MS 1330	D. M. Small	5348
1	MS 1330	D. C. Sprauer	5348
1	MS 1330	A. D. Sweet	5348
1	MS 0519	D. L. Bickel	5354
1	MS 0519	J. T. Cordaro	5354
1	MS 0519	J. DeLaurentis	5354
2	MS 9018	Central Technical Files	8944
2	MS 0899	Technical Library	4536

;-)